

WHISTLER MODE TURBULENCE AT EARTH'S BOW SHOCK:  
GENERATION VIA ELECTRON BEAMS AND  
RAY PATH INTEGRATED AMPLIFICATION

by

Robert Louis Tokar

A thesis submitted in partial fulfillment  
of the requirements for the Doctor of  
Philosophy degree in Physics  
in the Graduate College of  
The University of Iowa

December 1983

Thesis supervisor: Professor Donald A. Gurnett

Graduate College  
The University of Iowa  
Iowa City, Iowa

CERTIFICATE OF APPROVAL

PH.D. THESIS

This is to certify that the Ph.D. thesis of

Robert Louis Tokar

has been approved by the Examining Committee  
for the thesis requirement for the Doctor of  
Philosophy degree in Physics at the  
December 1983 graduation.

Thesis committee:

Donald Bennett  
Thesis supervisor

Stan H. Pfeiffer  
Member

Christopher K. L.  
Member

Paul Elango  
Member

M. Van Allen  
Member

## PREFACE

This study was conceived by Professor D. A. Gurnett at The University of Iowa and Dr. W. C. Feldman at the Los Alamos National Laboratory. I was introduced to the project on January 10, 1983, in Los Alamos, New Mexico. Detailed calculations performed in the first few months of 1983 produced new and exciting results that led to a theory for the generation of whistler mode turbulence at the bow shock. The initial results of the study are reported in Tokar et al. [1983]. A second paper that is in preparation, Tokar and Gurnett [1984], will present the ray path and amplification calculations for the waves.

I am grateful to Professor D. A. Gurnett for his guidance and support throughout this study. I also wish to thank Drs. W. C. Feldman and S. P. Gary at Los Alamos for many helpful discussions, and Ms. Kathy Goodner for skillfully preparing this manuscript.

This research was supported by NASA through Grants NGL-16-001-002 and NGL-16-001-043 from NASA Headquarters and Contract NAS5-26819 from Goddard Space Flight Center and by the Office of Naval Research through Contract N00014-76-C-0016.

## ABSTRACT

In this study the Landau and cyclotron growth rates of whistler mode instabilities in the transition region of Earth's bow shock are calculated using three electron distribution functions measured by the fast plasma experiment on ISEE 2 and a model distribution that is a function of penetration into the shock. An important feature of these electron distribution functions is the presence of a field-aligned beam with a  $T_{\perp} > T_{\parallel}$  anisotropy. The beam velocity vector is directed toward the magnetosheath. The calculations show that the distributions spontaneously generate whistler mode waves with electromagnetic Landau resonance and/or cyclotron resonance contributing to wave growth. Ray paths and path-integrated growth rates for the waves are calculated using a planar bow shock model. Waves with frequencies between about 1 and 100 Hz with a wide range of wave normal angles are generated by the Landau and anomalous cyclotron resonances. The ray paths for these waves are directed toward the magnetosheath. However, because the integrated growth rate is small the waves do not attain large amplitudes within the shock transition region. Waves with frequencies between about 30 and 150 Hz with a wide range of wave normal angles are generated by the normal cyclotron resonance. Waves generated near the center of the shock transition region in the frequency range from about 70 to 110 Hz attain large amplitudes. The ray paths for most of these



waves are directed toward the solar wind, although some wave packets, due to solar wind convection, travel transverse to the shock normal. These wave packets grow to large amplitudes because they spend a long time in the growth region. In the adopted planar bow shock model, the waves generated by the normal cyclotron resonance do not travel into the solar wind. The results of the study provide an explanation for the origin of much of the whistler mode turbulence observed at the bow shock.

## TABLE OF CONTENTS

	Page
LIST OF TABLES . . . . .	vi
LIST OF FIGURES . . . . .	vii
I. INTRODUCTION . . . . .	1
II. TRANSITION REGION ELECTRON DISTRIBUTION FUNCTIONS . . . . .	4
A. The Measured Distributions . . . . .	4
B. The Model Distribution . . . . .	9
III. METHOD OF CALCULATING THE GROWTH RATE . . . . .	17
IV. WHISTLER MODE INSTABILITY MECHANISMS . . . . .	23
A. Wave Vectors Directed Toward the Solar Wind: Generation Via the $m = -1$ Resonance . . . . .	25
B. Wave Vectors Directed Toward the Magnetosheath: Generation Via the $m = 0$ and $+1$ Resonances . . . . .	27
V. SUMMARY OF UNSTABLE FREQUENCIES AND WAVE NORMAL ANGLES . . . . .	31
A. The Measured Distributions . . . . .	31
B. The Model Distribution . . . . .	32
VI. PROPAGATION CHARACTERISTICS OF THE GENERATED WAVES . . . . .	36
A. Planar Bow Shock . . . . .	36
B. Ray Tracing Calculations . . . . .	38
VII. DISCUSSION . . . . .	48
VIII. CONCLUSION . . . . .	55
REFERENCES . . . . .	98

LIST OF TABLES

	Page
Table 1	
Parameters That Specify the Measured Velocity Distributions . . . . .	56
Table 2	
Shock Parameters For the Measured Velocity Distributions . . . . .	57

## LIST OF FIGURES

		Page
Figure 1	<p>This figure illustrates typical observations of whistler mode noise at the bow shock. The figure depicts data obtained with the ISEE-1 plasma wave experiment and the magnetic field experiment. The top panel shows the wave magnetic fields in ten frequency channels while the bottom panel illustrates the magnetometer data. The magnetic ramp defining the shock transition region is clearly visible as is the large amplitude whistler mode noise at the shock. The noise is most intense within the shock transition region and extends into the upstream solar wind and downstream magnetosheath. . . . .</p>	58
Figure 2	<p>This figure, reproduced from Feldman et al. [1982], shows parallel slices of electron distribution function data measured by the ISEE 2 fast plasma experiment. As the satellite moves from the solar wind into the</p>	

magnetosheath, field-aligned electron beams  
are observed. . . . . 60

Figure 3 This figure depicts contour plots of the  
logarithm of the analytic fits to the fast  
plasma experiment electron distribution  
function data analyzed in this study. These  
distribution functions were measured within  
the transition region of Earth's bow shock.  
A modified Lorentzian models the flat-topped  
component of the electron distribution and a  
convected Maxwellian with a  $T_{\perp} > T_{\parallel}$  aniso-  
tropy models the field-aligned electron  
beams. . . . . 62

Figure 4 This figure depicts the dependence on shock  
penetration of the convection speed of the  
Maxwellian component of the model distribu-  
tion. The convection speed is zero at the  
solar wind and increases to about  $6 \times 10^8$  cm/s  
at the magnetosheath. The increase in the  
convection speed is produced by a constant  
electric field within the transition region.  
The potential drop across the shock is taken  
to be 100 volts. . . . . 64

Figure 5

This figure depicts the increase in the electron plasma frequency with increasing shock penetration. This increase reflects the increase in the electron concentration measured by the fast plasma experiment on December 13, 1977. The plasma frequency increases from about 14 kHz at the solar wind to about 28 kHz at the magnetosheath. This variation with  $z$  of the plasma frequency is used in many calculations of this study. . . . . 66

Figure 6

This figure depicts the increase in the electron gyrofrequency with increasing shock penetration. This increase reflects the increase in the magnetic field magnitude measured by the magnetic field experiment on December 13, 1977. The gyrofrequency increases from about 140 Hz at the solar wind to about 560 Hz at the magnetosheath. This variation with  $z$  of the gyrofrequency is used in many calculations of this study. . 68

Figure 7

This figure depicts the variation with shock penetration of the perpendicular and parallel beam temperatures. The increase in the perpendicular temperature is consistent with conservation of the first adiabatic invariant of the electrons as the electrons move from the solar wind to the magnetosheath. The parallel temperature decreases from the solar wind value of  $1.5 \times 10^5 \text{K}$  to  $2 \times 10^4 \text{K}$  at the center of the transition region. This decrease is consistent with the December 13, 1977, measured distributions and is, by and large, attributable to the acceleration of the Maxwellian in the parallel direction. For  $z$  larger than 50 km, the parallel temperature is held constant. . . . . 70

Figure 8

This figure depicts contour plots of the logarithm of the model electron velocity distribution as a function of shock penetration,  $z$ . The distribution evolves from a relatively cool Maxwellian at the solar wind ( $z = 0 \text{ km}$ ) to a relatively hot modified

Lorentzian at the magnetosheath ( $z = 100$  km). As the beam energy increases, the anisotropy ratio,  $T_{\perp}/T_{\parallel}$ , increases as does the modified Lorentzian component of the model distribution. . . . . 72

Figure 9 The left column of this figure presents a sample of the growth rates obtained for the electron distribution function measured on December 13, 1977, at 17:35:55.7 UT. Plotted is the ratio of the total growth rate to real frequency. The growth rate is positive because the positive contribution of the  $m = -1$  resonance is larger than the negative contributions of the  $m = 0$  and  $+1$  resonances. The right column of this figure depicts the  $m = -1$  cyclotron resonance velocity as a function of wave normal angle for the two frequencies of interest. . . . . 74

Figure 10 In this figure, the range in the  $m = -1$  cyclotron resonance velocity corresponding to instability for  $\omega_r/2\pi = 110$  Hz, as obtained from Figure 2, is overlaid on a contour plot of the electron distribution



function measured on December 13, 1977, at  
 17:34:55.7 UT. The  $m = -1$  cyclotron reso-  
 nance velocities lie in regions of large  
 anisotropy,  $\frac{\partial F}{\partial \alpha} < 0$ . . . . . 76

Figure 11

The left column of this figure presents a  
 sample of the growth rates obtained for the  
 electron distribution function measured on  
 October 15, 1978, and for the frequency  
 $\omega_r/2\pi = 80$  Hz. The unstable waves have  $k_{\parallel} < 0$ ,  
 corresponding to wave vectors directed  
 toward the magnetosheath. The top left  
 panel shows the  $m = 0$  Landau contribution to  
 the growth rate while the bottom left panel  
 shows the  $m = +1$  cyclotron contribution to  
 the growth rate. For this frequency and  
 these wave normal angles the  $m = -1$  cyclo-  
 tron contribution to  $\omega_i/\omega_r$  is negative and  
 negligible. The right column depicts both  
 the  $m = 0$  Landau resonance velocity and the  
 $m = +1$  cyclotron resonance velocity as a  
 function of the wave normal angle. . . . . 78

Figure 12

In this figure, the range in the  $m = 0$   
 Landau and the  $m = +1$  cyclotron resonance

velocities corresponding to instability for  
 the case  $\omega_r/2\pi = 80$  Hz, as obtained from  
 Figure 4, is overlaid on a contour plot of  
 the electron distribution function measured  
 on October 15, 1978. The  $m = 0$  Landau  
 resonance velocities lie in regions of  
 positive  $\frac{k_{\parallel}}{|k_{\parallel}|} \frac{\partial F}{\partial v_{\parallel}}$  while the  $m = +1$  cyclotron  
 resonance velocities lie in a region of  
 large anisotropy,  $\frac{\partial F}{\partial \alpha} > 0$ . . . . . 80

Figure 13

This figure depicts the unstable frequencies  
 and wave normal angles for the October 15,  
 1978, measured distribution and the case of  
 generation via the  $m = 0$  and  $+1$  resonances.  
 A broad spectrum of frequencies, ranging  
 from about 1 to 100 Hz, is unstable. The  
 unstable wave normal angles range from  $0^\circ$  to  
 the resonance cone angle. For a given  
 frequency, the range of unstable wave normal  
 angles is consistent with locating the  
 resonance velocities in the free energy  
 regions of the distribution. . . . . 82

Figure 14

This figure depicts the unstable frequencies  
 and wave normal angles for the three

measured distributions and the case of generation via the  $m = -1$  resonance. In many cases, for a given frequency a wide range of wave normal angles is unstable. The unstable frequencies and wave normal angles locate the normal cyclotron resonance velocity in regions of anisotropy associated with the electron beam. . . . . 84

Figure 15

This figure summarizes the unstable frequencies as a function of shock penetration for the model distribution and generation via the  $m = 0$  and  $+1$  resonances. It is usually the case that for a given frequency a wide range of wave normal angles is unstable. The distribution is stable for  $z$  greater than about 50 km because  $\frac{k_{\parallel}}{|k_{\parallel}|} \frac{\partial F}{\partial v_{\parallel}}$  evaluated at the Landau resonance velocity is not sufficiently positive. . . . . 86

Figure 16

This figure summarizes the unstable frequencies as a function of shock penetration for the model distribution and generation via the  $m = -1$  resonance. The increase in frequency with increasing  $z$  is due to the fact

that the normal cyclotron resonance velocity must remain in regions of large anisotropy in  $F(z)$ . As in the case of the measured distributions, for many of the unstable frequencies a wide range of wave normal angles is unstable. . . . . 88

Figure 17

This figure depicts the planar bow shock model used in the ray tracing calculations. The shock transition region extends for 100 km in the  $\hat{z}$  direction and separates the upstream solar wind from the downstream magnetosheath. Within the shock transition, the plasma flow velocity is taken to be the solar wind velocity,  $\vec{v}_{sw} = 400 \hat{z}(\text{km/s})$ . The upstream angle between the magnetic field and the shock normal is taken to be  $45^\circ$ . Due to the planar geometry, the component of  $\vec{B}$  in the direction of  $\hat{n}$  is constant throughout the transition region. The magnetic field magnitude increases linearly with increasing  $z$ . A magnetic field line is shown as are  $B(z)$  and  $\theta_{Bn}(z)$  at  $z = 70 \text{ km}$ . . . . . 90

Figure 18

This figure illustrates the relative orientations of the magnetic field vector, the wave vector, the group velocity, and the solar wind velocity for the case of  $k_{\parallel} < 0$ . All vectors lie in the plane of the figure. Of the cone of unstable wave vectors, two are distinguished by the angle  $\phi$  with the  $\phi = 0^\circ$  direction defined to be towards the solar wind. The  $\phi = 180^\circ$  orientation lies on the unstable cone and is  $180^\circ$  in azimuth from the  $\phi = 0^\circ$  orientation. For a given wave vector orientation, the ray path direction in the shock frame of reference is in the direction of the vector  $\vec{v}_g + \vec{v}_{sw}$ . For  $k_{\parallel} < 0$ , the ray paths are directed toward the magnetosheath. . . . . 92

Figure 19

This figure is similar to Figure 19 but illustrates the geometry for the case  $k_{\parallel} > 0$ . The ray path directions in the shock frame are given by the direction of the vector  $\vec{v}_g + \vec{v}_{sw}$ . In the majority of cases, the ray path is directed toward the solar wind. However, the figure illustrates that for oblique wave normal angles and the  $\phi = 180^\circ$

orientation the ray path can be in the  
direction of the solar wind. . . . . 94

Figure 20

This figure summarizes the results of the ray tracing calculations. Shown are a magnetic field line and several ray paths in the shock transition region. The ray paths for generation via the  $m = 0$  and  $+1$  resonances originate in the lower left corner of the figure while those for generation via the  $m = -1$  resonance originate on the right side of the figure. The ray paths are labeled in the format  $(\omega_r/2\pi, \theta_0, \phi)$  where  $\theta_0$  and  $\phi$  specify the initial wave vector orientation. A  $\phi$  value for  $\theta_0 = 0^\circ$  is not applicable and so is omitted from the ray path labels. At the heads of the arrows denoting the ray path, the integrated growth along the ray path,  $\Gamma$ , is given. The ray paths terminate when the growth rate becomes negative. . . . . 96

## I. INTRODUCTION

Although shock waves in collisionless plasmas have been studied for more than two decades, the physics of collisionless shocks is still not well understood. Much of the current theoretical effort is aimed at formulating models that self-consistently describe the observed shock structures and the shock dissipation mechanisms. In a collisionless shock wave the upstream unshocked plasma is transformed into the downstream shocked plasma within a spatial length that is smaller than the mean free paths of the plasma particles. The region separating the upstream and downstream plasmas within which the dissipation occurs is called the shock transition region. Observations of fluctuating electric and magnetic fields associated with collisionless shocks in the laboratory and in interplanetary space indicate that plasma wave turbulence plays an important role in electron and ion heating at the shock. For additional reading on collisionless shocks, the review by Greenstadt and Fredericks [1979] provides a good starting point.

Earth's bow shock, the shock wave formed by the interaction of the solar wind with Earth's magnetic field, provides an excellent laboratory for the study of collisionless shock waves. The characteristics of the bow shock are highly variable because the parameters that characterize the upstream solar wind vary over a broad range. In addition, because spacecraft instruments have dimensions smaller than the

characteristic shock scale lengths, the shock fine structure can be studied in detail if high time resolution instrumentation is used or if the spacecraft is moving slowly with respect to the shock.

For many years it has been known that intense whistler mode turbulence exists at the bow shock [Holzer et al., 1966; Fredricks et al., 1968]. The noise is identified as whistler mode noise because it is electromagnetic noise at frequencies below the electron gyrofrequency and because the electric field to magnetic field ratio is in agreement with the ratio expected for the whistler mode [Rodríguez and Gurnett, 1975].

Typical observations of whistler mode turbulence at the bow shock are shown in Figure 1. In the top panel observations of the wave magnetic fields, obtained by the plasma wave experiment on the ISEE 1 satellite, are shown in ten frequency channels covering the range 5.6 Hz to 1 kHz and the time period 17:30:00.0 to 17:40:00.0 UT on December 13, 1977. The bottom panel depicts the magnetic field magnitude, measured by the magnetic field experiment on ISEE 1, over the same time period. The magnetic field data was provided through the courtesy of Dr. C. T. Russell at UCLA. The magnetic ramp defining the shock transition region is clearly visible, with upstream boundary at about 17:35:05.0 UT. At this time, the satellite enters the shock from the solar wind.

Whistler mode turbulence is clearly visible in the bottom six frequency channels of the wave magnetic field data shown in Figure 1. The noise exists over the broad frequency range of about 5.6 to 100 Hz, is



most intense in the shock transition region, and extends into the upstream solar wind and downstream magnetosheath.

The purpose of this study is to provide an explanation for the origin of much of the whistler mode turbulence in the transition region of the bow shock. The hypothesis is that electron beams with  $T_{\perp} > T_{\parallel}$  anisotropies that exist in the shock transition region and are moving toward the magnetosheath generate whistler mode instabilities via Landau and cyclotron resonance. The wave packets generated by the normal cyclotron resonance attain the large amplitudes typical of whistler mode waves at the bow shock.

This study makes use of data obtained with the ISEE 1 and 2 fast plasma experiment [Bame et al., 1978], plasma wave experiment [Gurnett et al., 1978] and magnetic field experiment [Russell, 1978]. The fast plasma experiment consists of spherical-section electrostatic analyzers that measure the electron velocity distribution over the energy range 5 eV to 14 keV. The ISEE plasma wave receivers use electric dipole and magnetic search coil antennas to measure wave electric and magnetic fields over the frequency range of about 5 Hz to 300 kHz. The ISEE magnetic field experiment uses a triaxial flux gate magnetometer to measure the magnetic field magnitude and direction. The individual reports cited above for each of these experiments provide detailed descriptions of the instrumentation.

## II. TRANSITION REGION ELECTRON DISTRIBUTION FUNCTIONS

The electron distribution functions analyzed in this study are based on distribution functions measured by the fast plasma experiment within the transition region of Earth's bow shock. In many instances, it is possible to fit the data obtained by the fast plasma experiment to simple analytic functions. This fitting procedure is described in Feldman et al. [1983]. Three analytic fits to measured data, provided by Dr. W. C. Feldman at the Los Alamos National Laboratory, are analyzed. In addition, a model electron distribution function that is a function of position within the shock transition region is constructed such that its features are consistent with reported experimental results. These two sets of distributions will be referred to as the measured distributions and the model distribution. In this section, the features of the measured distribution functions are described and the construction of the model distribution is discussed.

### A. The Measured Distributions

The fast plasma experiment is specifically designed to measure distribution functions in one dimension in approximately 100 milliseconds and distribution functions in two dimensions in one spin period (3 seconds). In particular, the time resolution of the fast plasma experiment is sufficient to allow measurements of distinct features of

electron distribution functions within the shock transition region with negligible aliasing of time. An important new feature of the electron distribution functions measured by the fast plasma experiment within the shock transition region is a field-aligned beam moving toward the magnetosheath [Feldman et al., 1982; 1983]. The beam is observed for both quasi-parallel and quasi-perpendicular turbulent shocks. Quasi-parallel and quasi-perpendicular refer to the angle between the shock normal and the magnetic field at the shock,  $\theta_{Bn}$ . For a quasi-parallel shock,  $\theta_{Bn}$  is greater than  $0^\circ$  but less than about  $45^\circ$  while for a quasi-perpendicular shock,  $\theta_{Bn}$  is greater than about  $45^\circ$  but less than  $90^\circ$ .

Figure 2 is reproduced from Feldman et al. [1982] and illustrates typical observations of the field-aligned electron beam. Shown in the figure are slices of electron distribution functions measured along the direction of the magnetic field by the ISEE 2 fast plasma experiment on December 13, 1977. The parallel slices of the distribution function were obtained in the solar wind (SW), in the shock transition region, and in the magnetosheath (MS). Data for the full two-dimensional electron distribution function obtained with the fast plasma experiment suggests that the solar wind electron distribution function at this time is a nearly isotropic Maxwellian and that the magnetosheath electron distribution function is a nearly isotropic modified Lorentzian. As the satellite enters the shock transition region, field-aligned electron beams are observed. The beams are moving toward the magnetosheath and the beam velocity increases with increasing shock

penetration. This figure supports the fact that the electron distribution functions measured in the shock transition region have both a flat-topped component and a beam component.

The analytic representation of the electron distribution function in the plasma rest frame,  $F(v_{\perp}, v_{\parallel})$ , is constructed from two measurements of the electron distribution function in planes parallel ( $v_{\parallel}$ ) and perpendicular ( $v_{\perp}$ ) to the ambient magnetic field separated in time by about 0.75 sec. Measurements of the electron distribution function in planes other than those parallel and perpendicular to the magnetic field confirm that the fits to these two data sets yield, for the purposes of this study, a sufficiently accurate representation of  $F(v_{\perp}, v_{\parallel})$ . The simple analytic function used to fit the data is a sum of a convected Maxwellian and a modified Lorentzian. The convected Maxwellian models the electron beam and the modified Lorentzian models the flat-topped component of the electron distribution function. These models provide excellent fits to both the parallel and the perpendicular slices of the distribution function.

Specifically,  $F(v_{\perp}, v_{\parallel})$  is given by

$$F(v_{\perp}, v_{\parallel}) = F_1 + F_2 \quad (1)$$

where

$$F_1 = \frac{C_1}{\left(1 + \left(\frac{(v_{\parallel} - v_1)^2 + v_{\perp}^2}{v_2^2}\right)^{P/R}\right)} \quad (2)$$

is the modified Lorentzian and

$$F_2 = C_2 \exp\left(-\frac{m(v_{\parallel} - v_3)^2}{2\kappa T_{\parallel}}\right) \exp\left(-\frac{m v_{\perp}^2}{2\kappa T_{\perp}}\right) \quad (3)$$

is the convected Maxwellian. In these equations,  $P$  and  $R$  are real numbers,  $T_{\perp}$  and  $T_{\parallel}$  are perpendicular and parallel temperatures,  $m$  is the electron mass,  $\kappa$  is Boltzman's constant, and  $C_1$ ,  $C_2$ ,  $v_1$ ,  $v_2$  and  $v_3$  are constants.

It should be noted that for the electron distribution functions analyzed in this study, the direction of positive  $v_{\parallel}$ , be it parallel or anti-parallel to the magnetic field, is determined by the bow shock geometry at the observation time. The positive  $v_{\parallel}$  direction is defined to be such that  $\hat{v}_{\parallel} \cdot \hat{n}$  is positive, where  $\hat{v}_{\parallel}$  is a unit vector in the positive  $v_{\parallel}$  direction and  $\hat{n}$  is a unit vector in the direction of the shock normal and toward the solar wind. Consequently, because the beam velocity vectors are always directed toward the magnetosheath, the convection speed,  $v_3$ , is always negative.

With the exception of the perpendicular beam temperature,  $T_{\perp}$ , the parameters in Equations 2 and 3 that specify the three measured electron distribution functions analyzed in this study are obtained from the fits to the fast plasma experiment data. The perpendicular beam temperature is not obtained from the fits to the data because, due to the relative motion of the spacecraft and the shock,  $T_{\perp}$  is not expected

to remain constant during the time it takes for the detector to rotate from the parallel to the perpendicular orientations. Consequently,  $T_{\perp}$  is calculated assuming that the first adiabatic invariant of the electrons is conserved as the electrons move from the solar wind into the shock. When the relative motion between the spacecraft and the bow shock is sufficiently slow so that  $T_{\perp}$  can be obtained, the calculated and measured perpendicular beam temperatures are in good agreement.

In Figure 3, contour plots of the best-fitting analytic models for the three sets of electron distribution function data measured by the ISEE 2 fast plasma experiment within the transition region of Earth's bow shock are shown. Plotted are contours of constant  $\log_{10} F(v_{\perp}, v_{\parallel})$  spanning one order of magnitude of  $F$ . The convected Maxwellians with  $T_{\perp} > T_{\parallel}$  anisotropies that model the electron beams are clearly visible as is the flat-topped feature of the modified Lorentzians. Two of the distributions shown were measured on December 13, 1977, and one was measured on October 15, 1978. In Table 1 the constants that specify the three measured electron distribution functions are listed, and in Table 2 the bow shock parameters at the three observation times are summarized.

The two distributions measured on December 13, 1977, correspond closely to the distributions measured at 17:34:55.8 and 17:34:58.6 UT that are depicted in Figure 2. Using the observation times and Figure 1, these distributions can be located with respect to the ramp in the magnetic field magnitude. However, Figure 1 depicts ISEE 1 data while Figure 2 depicts ISEE 2 data. This is because for the event

studied wave magnetic field data was only available from ISEE 1. The spatial separation of the two satellites is small. By comparing the ISEE 1 and ISEE 2 magnetic field profiles at these times, the temporal separation of the two data sets is found to be about 15 seconds. For example, the time 17:35:00.0 UT on ISEE 2 corresponds to 17:35:15.0 UT on ISEE 1. These facts lead to the conclusion that the December 13, 1977, velocity distributions were measured near the center of the magnetic ramp or shock transition region.

It turns out that the electron distribution function measured on October 15, 1978, is unusual because the magnetic field magnitude at the observation time, 18:21:02.0 UT, is still at the upstream solar wind value. In contrast, the electron concentration has risen from its solar wind value. Because on the average these two quantities increase simultaneously at the shock [Bame et al., 1979], the distribution is atypical. It is included in this study because the beam energy is the smallest observed to date by the fast plasma experiment group. The properties of this distribution will not be used in the construction of the model distribution.

#### B. The Model Distribution

It is desirable to obtain a model electron distribution function that is a function of position within the shock transition region. Using such a velocity distribution, the generation of whistler mode waves throughout the transition region can be studied in detail. In this study, a simple model electron distribution function is constructed such that its features are consistent with the velocity



distributions measured on December 13, 1977, and reported experimental results. An alternative approach would be to solve the Vlasov-Maxwell equations throughout the transition region. While such a solution would possess a self-consistency absent in the simple model adopted, obtaining an accurate solution would be a long and complex task. Consequently, the program adopted is to construct a simple model that agrees with experimental findings.

Referring to Equations 2 and 3 it is observed that to construct the distribution function as a function of position within the shock transition region the following nine parameters must be known as a function of position within the shock transition region:  $C_1$ ,  $C_2$ ,  $v_1$ ,  $v_2$ ,  $v_3$ ,  $P$ ,  $R$ ,  $T_{\parallel}$ , and  $T_{\perp}$ . To construct functions that describe the variation of these parameters within the shock transition region the following observational facts are employed.

- 1) As the transition region is traversed by the spacecraft, the electron distribution function evolves from the upstream solar wind distribution to the downstream magnetosheath distribution. A typical solar wind electron distribution function is an isotropic Maxwellian with a temperature of about  $1.5 \times 10^5$  K. A typical magnetosheath electron distribution function is a modified Lorentzian with  $P \approx 4.0$ ,  $R \approx P-1$  and  $v_2 \approx 6 \times 10^8$  cm/s [Feldman et al., 1983].
- 2) On the average, both the electron concentration and the magnetic field magnitude begin to increase at the shock and



continue to increase with increasing penetration into the shock transition region [Bame et al., 1979]. For the shock crossings measured on December 13, 1977, the electron concentration increased from about  $2.5 \text{ cm}^{-3}$  to about  $10 \text{ cm}^{-3}$  (W. C. Feldman, personal communication) and the magnetic field magnitude increased from about 5 gammas to about 20 gammas (C. T. Russell, personal communication).

- 3) The convection speed of the beam,  $v_3$ , increases with increasing shock penetration. The increase is consistent with the interpretation that the incoming solar wind electrons are accelerated by a macroscopic electric field within the shock transition region [Feldman et al., 1983]. Potential drops across the bow shock are on the order of one to a few hundred volts [Formisano, 1980]. An average thickness of the shock transition region is 100 km [Russell, 1979].
- 4) The electron distribution functions in the shock transition region have a flat ledge in the direction opposite to the beam. The corner of the ledge is located at a speed approximately equal to the beam speed,  $v_3$  [Feldman et al., 1983].
- 5) The electron distribution functions measured on December 13, 1977, and shown in Figure 3 have a parallel beam temperature of about  $2 \times 10^4 \text{ K}$ . These distributions were measured near the center of the shock transition region.

Consistent with these facts, the following simple functions are chosen to describe the evolution of the electron distribution function from the solar wind to the magnetosheath. In the equations,  $z$  denotes penetration length along the shock normal and into the shock transition region. The position  $z = 0$  is the upstream solar wind boundary.

$$\begin{aligned} \text{a) } C_1 &= 1 - (z/100.) & z \text{ in kilometers} \\ C_2 &= z/100. \end{aligned} \tag{4}$$

These simple equations serve to describe the evolution of the distribution function from the initial solar wind Maxwellian to the magnetosheath modified Lorentzian. In agreement with point 1 above, the distribution function evolves from a Maxwellian in the solar wind ( $z = 0$ ) to a modified Lorentzian in the magnetosheath ( $z = 100$  km). The thickness of the shock transition region, 100 km, agrees with point 3 above.

It should be noted that the units for  $C_1$  and  $C_2$  are chosen to be arbitrary. The electron distribution function must be multiplied by an additional constant to ensure that its integral over all velocity space equal the electron concentration, which is also a function of position within the transition region. Of course, the units for this normalization constant are not arbitrary.

$$b) \quad v_3 = \sqrt{\frac{2e\phi(z)}{m}} \quad \phi(z) = (z/100)(100 \text{ volts})$$

$$v_2 = v_3 \quad (5)$$

$$v_1 = 0$$

In these equations,  $e$  is the electronic charge and  $m$  is the electron mass.

The simple equation for the convection speed,  $v_3$ , represents uniform acceleration produced by a constant electric field of magnitude  $1 \times 10^{-3}$  v/m within the transition region. A potential drop of 100 volts across the bow shock results in convection speeds within the shock transition region consistent with the measured electron distributions shown in Figure 3 and a modified Lorentzian in the magnetosheath with a breakpoint speed of about  $6 \times 10^8$  cm/s. These points are illustrated in Figure 4, where  $v_3$  is plotted as a function of  $z$ . The adopted expression for  $v_3$  and the equation  $v_2 = v_3$  satisfy points 3 and 4 above. The condition  $v_1 = 0$  is adopted to avoid computational difficulty and means that the modified Lorentzian is always centered about zero velocity.

$$c) \quad P = 4$$

$$(6)$$

$$R = 3$$

These values are typical of magnetosheath electron distribution functions measured by the fast plasma experiment and reported by Feldman et al. [1983].

$$\begin{aligned} \text{d) } n_e(z) &= n_0 + .075 z \quad \text{in cm}^{-3} & n_0 &= 2.5 \text{ cm}^{-3} \\ B(z) &= B_0 + .15 z \quad \text{in gammas} & B_0 &= 5 \text{ gammas} \end{aligned} \quad (7)$$

These equations represent ramps in the electron concentration and magnetic field magnitude and are consistent with point 2 above. As a result, the electron plasma frequency,  $\omega_p/2\pi$ , increases from about 14 kHz at the solar wind to about 27 kHz at the magnetosheath. The electron gyrofrequency,  $\omega_g/2\pi$ , increases from about 140 Hz at the solar wind to 560 Hz at the magnetosheath. The variation with  $z$  of the electron plasma frequency and the electron gyrofrequency is illustrated in Figures 5 and 6, respectively.

$$\text{e) } T_{\perp} = (B(z)/B_0) 1.5 \times 10^5 \text{ K} \quad (8)$$

This equation expresses the conservation of the first adiabatic invariant of the electrons as the electrons move from the solar wind into the shock. The expression for  $B(z)$  and the value of  $B_0$  are given in Equation 7.

$$f) \quad T_{\parallel} = \begin{cases} 1.5 \times 10^5 \text{K} - \left( \frac{1.5 \times 10^5 - 2 \times 10^4}{50 \text{ km}} \right) z & z < 50 \text{ km} \\ 2 \times 10^4 \text{K} & z > 50 \text{ km} \end{cases} \quad (9)$$

These equations reduce  $T_{\parallel}$  from the typical solar wind value of  $1.5 \times 10^5 \text{K}$  to  $2 \times 10^4 \text{K}$  at the center of the shock, in agreement with point 5 above. For distances from the solar wind side of the shock greater than 50 km, the parallel temperature of the beam is held constant at  $2 \times 10^4 \text{K}$  to avoid computational difficulty. This simplifying assumption has a negligible effect on the calculations of this study because for large shock penetrations the features of the electron distribution are primarily those of the modified Lorentzian.

In general, the reduction in  $T_{\parallel}$  is due to the fact that the Maxwellian is being accelerated by an electric field in the parallel direction. However, the parallel electric field in the transition region required to reduce  $T_{\parallel}$  to  $2 \times 10^4 \text{K}$  at  $z = 50 \text{ km}$  is about  $.2 \times 10^{-3} \text{ v/m}$  and not the  $1 \times 10^{-3} \text{ v/m}$  used to model the convection speed. Rather than use two different electric field magnitudes to model  $v_3$  and  $T_{\parallel}$ , the crude function given in Equation 9 is adopted. In Figure 7,  $T_{\perp}$  and  $T_{\parallel}$  are shown as a function of shock penetration.

Equations 1 through 9 define the electron distribution function throughout the shock transition region. Contour plots of the base 10 logarithm of the model distribution function, spanning one order of magnitude of  $F$ , are shown in Figure 8 for six positions within the shock transition region. This figure illustrates that the distribution

function evolves from a relatively cool solar wind Maxwellian ( $z = 0$  km) to a hotter magnetosheath modified Lorentzian ( $z = 100$  km) in a continuous fashion. As the Maxwellian gains energy in the parallel direction, the temperature ratio of the Maxwellian,  $T_{\parallel}/T_{\perp}$ , increases in magnitude as does the modified Lorentzian component of the model distribution.

### III. METHOD OF CALCULATING THE GROWTH RATE

In this study, an expression for the growth rate of electromagnetic plasma waves given by Kennel and Wong [1967] is employed. Kennel and Wong [1967] derived this expression in the weak damping limit using the linearized Vlasov and Maxwell equations. It can be shown that the expression given by Kennel and Wong is equivalent to the growth rate expression in Kennel [1966].

Although the Kennel and Wong expression contains an infinite sum over resonances, only the Landau and first-order cyclotron resonance contributions to the growth rate are retained. This approximation is justified because few electrons exist at the higher order resonance velocities. An additional simplifying assumption is to neglect the motion of the ions. This simplification is justified because it is expected that all ions in the regions under consideration have velocities less than the wave phase velocities characteristic of this study.

With these approximations, Kennel and Wong's expression for the growth rate,  $\omega_i$ , is given by the equation

$$\omega_i = |\omega_r| \text{sign}\left(\frac{\omega_r}{k_{\parallel}}\right) \frac{\omega_p^2}{2\omega_r} \frac{\pi}{16} \int_0^{\infty} v_{\perp}^2 (I_{-1} + I_0 + I_1) dv_{\perp} \quad (10)$$

where

$$I_m = \frac{[\epsilon_L J_{m-1}(x) + \epsilon_R J_{m+1}(x) - \sqrt{2}(\frac{v_{\parallel}}{v_{\perp}}) \epsilon_{\parallel} J_m(x)]^2 (v_{\perp} \frac{\partial F}{\partial v_{\parallel}} - \frac{m\omega_g}{k_{\parallel}} \frac{\partial F}{\partial v_{\perp}})}{W} \bigg|_{v_{\parallel} = \frac{\omega_r + m\omega_g}{k_{\parallel}}}$$

and  $W$ , the total wave energy, is given by

$$W(\vec{k}, \omega) = \frac{1}{16\pi} [\vec{B}^*(\vec{k}, \omega) \cdot \vec{B}(\vec{k}, \omega) + \vec{E}^*(\vec{k}, \omega) \cdot (\frac{\partial}{\partial \omega} \omega \vec{K}^h) \cdot \vec{E}(\vec{k}, \omega)]$$

In these equations,  $F$  is the electron distribution function normalized to unity,  $\omega_r$  is the real frequency of the wave,  $k$  is the wave number,  $\epsilon_L$ ,  $\epsilon_R$ , and  $\epsilon_{\parallel}$  are the left-hand, right-hand, and parallel electric field polarization vectors of the wave,  $\vec{K}^h$  is the Hermitian part of the dielectric tensor,  $\omega_g$  is the absolute value of the electron gyro-frequency, and  $x$  is  $\frac{v_{\perp}}{\omega_g}$ . The Landau contribution to the growth rate is the  $m = 0$  term and the normal and anomalous cyclotron resonance contributions are given by the  $m = -1$  and the  $m = +1$  terms. A positive growth rate indicates exponential growth and a negative growth rate indicates exponential damping.

It should be noted that this expression for the growth rate is derived assuming that  $\omega_i/\omega_r \ll 1$ . It turns out that some of the growth rates calculated in this study do not satisfy this condition. When



this condition is not met, the growth rate calculated using Equation 9 is not accurate. While this difficulty does point out the fact that some of the growth rates calculated in this study are rough estimates, the signs of the calculated growth rates are always correct. Thus, the stability or instability of the distribution function is never in doubt. In addition, at no point in this study is a value for  $\omega_i/\omega_r$  greater than .5 used in a calculation.

In order to employ Equation 1 to calculate growth rates for whistler mode waves, the real part of the whistler mode dispersion relation must be solved for  $\omega_r$  as a function of  $k$ . For simplicity, this study assumes that the real part of the whistler mode dispersion relation is that of a cold plasma. In this approximation, analytic expressions for  $\epsilon_R$ ,  $\epsilon_L$ ,  $\epsilon_{\parallel}$ , and  $W$  are easily derived. They are

$$\epsilon_R = \frac{n^2 - S + D}{\sqrt{2}(n^2 - S)} \quad (11)$$

$$\epsilon_L = \frac{n^2 - S - D}{\sqrt{2}(n^2 - S)} \quad (12)$$

$$\epsilon_{\parallel} = \frac{n^2 \cos \theta \sin \theta}{n^2 \sin^2 \theta - P} \quad (13)$$

and

$$\begin{aligned}
 W = \frac{1}{16\pi} & \left[ \left( \frac{n^2 \cos \theta \sin \theta}{n^2 \sin^2 \theta - P} \right)^2 \left( \frac{P^2}{n^2 \sin^2 \theta} - P \right) + \frac{D^2}{(S - n^2)^2} \left( n^2 + S - \frac{2S^2}{P} \right) \right. \\
 & \left. + \frac{2D}{n^2 - S} \left( D + \frac{2\omega \omega_g S^2}{\omega_p^2} - \frac{\omega_g S}{\omega} \right) + S - \frac{2S^2}{P} \right] \quad .
 \end{aligned} \tag{14}$$

In these equations,  $n = ck/\omega_r$  is the index of refraction for the mode under consideration,  $\theta$ , the wave normal angle, is the angle between the wave vector and the magnetic field and  $S$ ,  $D$ , and  $P$  are quantities first introduced by Stix [1962]. When specializing to the whistler mode, for the frequencies of interest in this study these quantities are given to good approximation by the equations

$$n = \frac{ck}{\omega_r} = \frac{\omega_p}{\omega_r^{1/2} (\omega_g \cos \theta - \omega_r)^{1/2}} \tag{15}$$

$$S = \frac{\omega_p^2}{(\omega_g - \omega_r)(\omega_g + \omega_r)} \tag{16}$$

$$D = \frac{\omega_g}{\omega_r} S \tag{17}$$

and

$$P = \frac{-\omega_p^2}{\omega_r^2} \quad . \quad (18)$$

Combining Equations 10 through 18, an approximate but tractable expression for the growth rate is obtained.

It is desirable to investigate in at least a semi-quantitative way the validity of the simplifying assumption that the real part of the whistler mode dispersion relation is that of a cold plasma. When the wave phase velocity is much greater than the electron thermal speed, it is known that hot plasma effects on the dispersion relation of the whistler mode are small (e.g., see Leimohn [1962]). However, in the work reported here the wave phase velocities are often comparable to the electron thermal velocities. To investigate the error introduced, the numerical code of Forslund [1979], which solves the fully electromagnetic linear dispersion relation for a plasma that is a sum of Maxwellian distributions, has been utilized to determine the real frequency,  $\omega_r$ , for a given wave number,  $k$  [S. P. Gary, personal communication]. For parameters typical of this study, the results indicate that for a given wave number and for wave normal angles  $\theta \leq 45^\circ$ , the real frequency for a cold plasma and the real frequency obtained using the code of Forslund differ by not more than 30 percent. If  $k$  is held constant and  $\omega_r$  is allowed to vary by 30 percent, the computations show that the change in the growth rate calculated using Equation 10 is, for the majority of unstable wave numbers, less than about 20%.

As the wave normal angle approaches the resonance cone angle,  $\theta_{\text{Res}} \approx \cos^{-1}(\frac{\omega_r}{\omega_g})$ , the index of refraction becomes infinite and the wave becomes predominantly electrostatic. For wave normal angles near the resonance cone angle, the difference between the real frequency for a cold plasma and the real frequency obtained using the code of Forslund for a given  $k$  is larger than it is for small wave normal angles. Consequently, it should be noted that while the primary results of this study are not affected by the simplifying assumption used in calculating the growth rate, the calculated growth rates for wave normal angles near  $\theta_{\text{Res}}$  are not accurate.

#### IV. WHISTLER MODE INSTABILITY MECHANISMS

Growth rates for whistler mode waves have been calculated using Equation 10 and the measured and model electron distribution functions depicted in Figures 3 and 8. The results indicate that these electron distribution functions are unstable to whistler mode waves. In this section, the growth mechanisms that generate the whistler mode instabilities are identified. To facilitate the discussion, the measured electron distribution functions shown in Figure 3 will be employed as examples to illustrate the generation mechanisms. These same generation mechanisms apply for the model distribution in the shock transition region. In the following section, the whistler mode instabilities generated by both the measured and the model distributions will be summarized.

From Equation 10 it is observed that the total growth rate is a sum of three terms: the two cyclotron resonance contributions and the Landau resonance contribution. The sign of the growth rate is positive if the sum of the three contributions is positive. The signs of the  $m = -1, 0$ , and  $+1$  contributions are positive or negative depending on whether or not the following quantity is positive or negative:

$$\text{sign}\left(\frac{\omega_r}{k_{\parallel}}\right) \int_0^{\infty} \left( v_{\perp} \frac{\partial F}{\partial v_{\parallel}} - \frac{m\omega_g}{k_{\parallel}} \frac{\partial F}{\partial v_{\perp}} \right) v_{\perp}^2 dv_{\perp} \bigg|_{v_{\parallel} = \frac{\omega_r + m\omega_g}{k_{\parallel}}} \quad (19)$$

which can be rewritten in the form

$$\text{sign}\left(\frac{\omega_r}{k_{\parallel}}\right) \int_0^{\infty} \left( v_{\perp} \frac{\partial F}{\partial v_{\parallel}} + \left( \frac{\omega_r}{k_{\parallel}} - v_{\parallel} \right) \frac{\partial F}{\partial v_{\perp}} \right) v_{\perp}^2 dv_{\perp} \bigg|_{v_{\parallel} = \frac{\omega_r + m\omega_g}{k_{\parallel}}} \quad (20)$$

Integrating the second term in Equation 20 by parts and introducing the electron pitch angle,  $\alpha$ , where  $\alpha$  is measured from the positive  $v_{\parallel}$  axis, Equation 20 can be rewritten as

$$\text{sign}\left(\frac{\omega_r}{k_{\parallel}}\right) \left[ -\frac{2\omega_r}{k_{\parallel}} \int_0^{\infty} F v_{\perp} dv_{\perp} - \int_0^{\infty} \frac{\partial F}{\partial \alpha} v_{\perp}^2 dv_{\perp} \right] \bigg|_{v_{\parallel} = \frac{\omega_r + m\omega_g}{k_{\parallel}}} \quad (21)$$

The whistler mode waves generated by the electron distribution functions shown in Figure 3 fall naturally into two categories: waves with wave vectors predominantly in the opposite direction of the beam velocity and waves with wave vectors predominantly in the direction of the beam velocity. For waves propagating in the direction opposite to the beam, i.e., toward the solar wind,  $k_{\parallel}$  is positive and the growth

mechanism is the normal  $m = -1$  cyclotron resonance. All three electron distribution functions shown in Figure 3 generate whistler mode waves via the  $m = -1$  normal cyclotron resonance. For waves propagating in the direction of the beam, i.e., toward the magnetosheath,  $k_{\parallel}$  is negative and the growth mechanisms are the  $m = 0$  Landau and the anomalous  $m = +1$  cyclotron resonance. Of the three electron distribution functions shown in Figure 3, only the distribution function measured on October 15, 1978, generates whistler mode waves propagating in the direction of the beam. In the following subsections, the cases  $k_{\parallel} > 0$  and  $k_{\parallel} < 0$  are examined.

A. Wave Vectors Directed Toward the Solar Wind:  
Generation Via the  $m = -1$  Resonance

To investigate the generation of whistler mode waves by the normal  $m = -1$  cyclotron resonance contribution to the growth rate, consider Equations 19 through 21 when  $m = -1$ . Because the beams depicted in Figure 3 are moving in the direction of the magnetosheath, the parallel component of the wave vector must be positive for interactions via the  $m = -1$  cyclotron resonance. For the distribution functions shown in Figure 3, the second term in Equation 19 is negative. Therefore, in order for Equation 19 to be positive,  $v_{\perp}^3 \frac{\partial F}{\partial v_{\parallel}}$  evaluated at the  $m = -1$  cyclotron resonance velocity,  $v_{\parallel} = \frac{\omega_r - \omega_g}{k_{\parallel}}$ , and integrated over all  $v_{\perp}$  must be sufficiently positive to overcome the negative term. Equivalently, Equation 21 expresses the result that a region of sufficiently large anisotropy,  $\frac{\partial F}{\partial \alpha} < 0$ , along the  $m = -1$  cyclotron resonance velocity must exist if the growth rate is to be positive.

From these facts it is expected that the electron distribution functions shown in Figure 3 will generate whistler mode waves if the cyclotron resonance velocity has a larger magnitude than the magnitude of the convection speed of the Maxwellian modelling the electron beam,  $|v_3|$ . In this region of the electron distribution functions shown in Figure 3,  $\frac{\partial F}{\partial v_{\parallel}}$  is positive and  $\frac{\partial F}{\partial \alpha}$  is negative.

The left column of Figure 9 shows representative growth rates obtained using the electron distribution function measured within the shock transition region at 17:34:55.7 UT on December 13, 1977. At this time,  $\frac{\omega_E}{2\pi}$  is about 315 Hz and  $\frac{\omega_P}{2\pi}$  is about 20 kHz. Plotted are the ratios of total growth rate,  $\omega_i$ , to real frequency,  $\omega_r$ , as a function of the wave normal angle. The growth rates for the two frequencies  $\omega_r/2\pi = 110$ , and 120 Hz are given. This figure depicts whistler mode waves with positive growth rates. The absence of a plotted growth rate indicates damping. For the frequencies shown here, both the  $m = +1$  cyclotron resonance and the  $m = 0$  Landau resonance contributions to  $\omega_i$  are negative and small compared to the positive contribution of the  $m = -1$  cyclotron resonance. The left column of Figure 9 indicates that as the frequency is increased the range of unstable wave normal angles decreases while the centroids of these angles, which range from 0 to about 80 degrees, increase. This trend can be understood from a plot of the  $m = -1$  cyclotron resonance velocity.

The right column of Figure 9 shows the  $m = -1$  cyclotron resonance velocity as a function of wave normal angle for the two frequencies



$\frac{\omega_r}{2\pi} = 110$  and  $120$  Hz. For the electron distribution function measured at 17:34:55.7 UT on December 13, 1977, the Maxwellian modelling the electron beam is convected into the shock at a speed of about  $3.255 \times 10^8$  cm/s. It is expected that the resonance velocity must have a larger negative value than  $-3.255 \times 10^8$  cm/s if instability is to occur as only then will  $\partial F / \partial \alpha$  be sufficiently negative (or  $\partial F / \partial v_{\parallel}$  sufficiently positive) along the integration path. This point is illustrated in Figure 10 where the resonance velocity range giving rise to instability for the case  $\frac{\omega_r}{2\pi} = 110$  Hz, as obtained from Figure 10, is overlaid on a contour plot of the electron distribution function measured at 1734:55.7 UT on December 13, 1977. The resonance velocity lies in a region of positive  $\frac{\partial F}{\partial v_{\parallel}}$  and large anisotropy,  $\frac{\partial F}{\partial \alpha} < 0$ .

#### B. Wave Vectors Directed Toward the Magnetosheath: Generation Via the $m = 0$ and $+1$ Resonances

To investigate the generation of whistler mode waves by the  $m = 0$  Landau and the  $m = +1$  anomalous cyclotron resonances, Equations 19 through 21 are again examined. Because the convection speeds for the electron beams shown in Figure 3 are negative, for the generation of whistler mode waves via the  $m = 0$  and the  $m = +1$  interactions  $k_{\parallel}$  is negative, corresponding to wave vectors directed toward the magnetosheath.

From Equation 19 it is seen that in order for the  $m = 0$  Landau contribution to  $\omega_i$  to be positive,  $-v_{\perp}^3 \frac{\partial F}{\partial v_{\parallel}}$  evaluated at the Landau resonance velocity,  $v_{\parallel} = \frac{\omega_r}{k_{\parallel}}$ , and integrated over all  $v_{\perp}$  must be

positive. Taking into account the sign of  $k_{\parallel}$  with the expression  $\frac{k_{\parallel}}{|k_{\parallel}|}$ , this will occur when regions of large positive  $\frac{k_{\parallel}}{|k_{\parallel}|} \frac{\partial F}{\partial v_{\parallel}}$  exist along the integration path. Considering the  $m = +1$  cyclotron term for the case when  $k_{\parallel}$  is negative, the first term in Equation 21 is negative. Consequently, the  $m = +1$  cyclotron resonance contribution to the growth rate will be positive when regions of large anisotropy,  $\frac{\partial F}{\partial \alpha} > 0$ , exist along the integration path.

Of the three electron distribution functions shown in Figure 3, only the distribution function measured on October 15, 1978, generates whistler mode waves via the  $m = 0$  and the  $m = +1$  resonances. This is because the convection speeds for the electron beams in the distribution functions measured on December 13, 1977, are large. Because the convection speeds are large,  $\frac{\partial F}{\partial v_{\parallel}}$  is near zero at typical Landau resonance velocities and the Landau contribution to the growth rate is small. Consequently, the  $m = -1$  cyclotron contribution to damping dominates any positive contribution to the growth rate due to the  $m = +1$  cyclotron resonance. This is not the case for the electron distribution function measured on October 15, 1978, which has a smaller beam velocity. Because the beam velocity is small, the  $m = 0$  Landau contribution to  $\omega_i$  is large and positive.

The left column of Figure 11 presents a sample of the growth rates obtained using the October 15, 1978, electron distribution function. The results are given for one frequency,  $\frac{\omega_r}{2\pi} = 80$  Hz. At this time,  $\frac{\omega_E}{2\pi}$  is about 110 Hz and  $\frac{\omega_p}{2\pi}$  is about 20 kHz. The top left panel shows the

$m = 0$  Landau resonance contribution to the ratio  $\frac{\omega_i}{\omega_r}$  while the bottom left panel gives the  $m = +1$  cyclotron resonance contribution to  $\frac{\omega_i}{\omega_r}$ . The  $m = -1$  cyclotron resonance contribution to  $\frac{\omega_i}{\omega_r}$  is negative and negligible for these wave normal angles and this frequency. The right column of Figure 11 depicts the Landau resonance velocity and the  $m = +1$  cyclotron resonance velocity as a function of wave normal angle for  $\frac{\omega_r}{2\pi} = 80$  Hz.

From Figure 11 it is observed that the Landau contribution to  $\omega_i$  is a maximum at an intermediate wave normal angle and decreases to zero at  $0^\circ$  and  $\theta_{\text{Res}}$  ( $\theta_{\text{Res}} \approx 43^\circ$  here). The contribution is positive over a wide range of wave normal angles because the Landau resonance velocity lies in a region of positive  $\frac{k_{\parallel}}{|k_{\parallel}|} \frac{\partial F}{\partial v_{\parallel}}$  over a wide range of wave normal angles. The Landau growth rate goes to zero at  $0^\circ$  because the whistler mode wave is purely transverse at that angle and goes to zero at  $\theta_{\text{Res}}$  because the index of refraction for the whistler mode becomes very large near  $\theta_{\text{Res}}$ , thereby moving the resonance velocity out of the region of large positive  $\frac{k_{\parallel}}{|k_{\parallel}|} \frac{\partial F}{\partial v_{\parallel}}$ .

The  $m = +1$  cyclotron resonance contribution to  $\omega_i$  is positive for wave normal angles between about  $10^\circ$  and  $42^\circ$ . The  $m = +1$  contribution falls to zero as the wave normal angle approaches  $0^\circ$  because  $I_{+1}$  in Equation 10 is identically zero at  $0^\circ$ . This corresponds to the fact that a parallel propagating whistler mode wave is right-hand polarized with respect to the magnetic field, whereas the anomalous  $m = +1$  resonance requires a left-hand polarization component for a resonant

interaction to occur. The  $m = +1$  contribution is zero for wave normal angles greater than about  $42^\circ$  because the  $m = +1$  cyclotron resonance velocity does not lie in a region of sufficiently positive  $\frac{\partial F}{\partial \alpha}$  for wave normal angles greater than  $42^\circ$ .

In Figure 12, the range of unstable resonance velocities for the  $m = 0$  and the  $m = +1$  resonances, as obtained from Figure 12, is overlaid on a contour plot of the October 15, 1978, electron distribution function. The Landau resonance velocity lies in a region of positive  $\frac{k_{\parallel}}{|k_{\parallel}|} \frac{\partial F}{\partial v_{\parallel}}$  while the  $m = +1$  cyclotron resonance velocity lies in regions of large anisotropy,  $\frac{\partial F}{\partial \alpha} > 0$ .

## V. SUMMARY OF UNSTABLE FREQUENCIES AND WAVE NORMAL ANGLES

Using Equation 10 and the analytic fits to the measured electron distribution data, shown in Figure 3, and the model electron distribution, defined by Equations 1 through 9, growth rates for whistler mode instabilities have been calculated. For the distributions shown in Figure 3, the growth rate is calculated as a function of wave frequency and wave normal angle. For the model distribution, the growth rate is calculated as a function of wave frequency, wave normal angle, and position within the shock transition region. These calculations identify the unstable (i.e.,  $\omega_i > 0$ ) plasma rest frame frequencies and wave normal angles of whistler mode instabilities in the shock transition region. In Section IV the generation mechanisms were identified and discussed. In this section, the unstable frequencies and wave normal angles are summarized.

### A. The Measured Distributions

The measured distributions, depicted in Figure 3, generate whistler mode instabilities via the three mechanisms outlined in Section IV. The distribution measured on October 15, 1978, generates waves with wave vectors directed toward the magnetosheath and with wave vectors directed toward the solar wind. Because the beam convection speeds for the distributions measured on December 13, 1977, are large,

these distributions only generate waves with wave vectors directed toward the solar wind.

Figures 13 and 14 summarize the unstable frequencies and wave normal angles for the electron distribution functions shown in Figure 3. Figure 13 depicts the waves that are generated by the  $m = 0$  and  $+1$  resonances for the October 15, 1978, velocity distribution. The frequencies and wave normal angles with  $\omega_1 > 0$  are indicated by the shading. These waves have  $k_{\parallel} < 0$ , corresponding to wave vectors directed toward the magnetosheath. This figure illustrates that a broad band of frequencies with a wide range of wave normal angles are generated by the  $m = 0$  and  $+1$  resonances. The decrease in the range of unstable wave normal angles near 50 Hz is due to the fact that the  $m = -1$  cyclotron damping is largest near 50 Hz.

The unstable frequencies and wave normal angles for generation via the  $m = -1$  resonance are shown in Figure 14. In the bottom panel, the results for the October 15, 1978, distribution are shown while the top panels correspond to the two December 13, 1977, distributions. These whistler mode waves are all generated by the  $m = -1$  cyclotron resonance term and have  $k_{\parallel} > 0$ . The frequency dependence of the unstable wave normal angles is consistent with the discussion in Section IV, part A.

#### B. The Model Distribution

For the model electron distribution function,  $F(z)$ , defined by Equations 1 through 9, the unstable frequencies and wave normal angles are a function of penetration into the transition region,  $z$ . This is because the evolution with  $z$  of the velocity distribution from an

isotropic Maxwellian at the solar wind to an isotropic modified Lorentzian at the magnetosheath causes the conditions for instability to be functions of  $z$ . Before presenting the unstable frequencies and wave normal angles for the model distribution, a brief discussion of how the evolution of the model distribution with  $z$  effects the conditions for instability is desirable.

In Section IV the instability conditions for the three generation mechanisms are discussed in detail. There it is shown that for generation via the  $m = 0$  Landau resonance, the distribution must possess a positive and sufficiently large  $\frac{k_{\parallel}}{|k_{\parallel}|} \frac{\partial F}{\partial v_{\parallel}}$  at the wave phase velocity. It is clear that as the Maxwellian component of  $F(z)$  evolves away from the  $v_{\parallel} = 0$  axis, this condition will be satisfied if  $z$  is less than about 50 km. As  $z$  increases from 50 km to 100 km, the parallel derivative of  $F(z)$  decreases to zero because the dominant component of  $F(z)$  is the isotropic modified Lorentzian. In Section IV it is also shown that for generation via the normal and anomalous cyclotron resonances the distribution must possess regions of sufficiently large anisotropy. In  $F(z)$ , this anisotropy is due to the increase in the beam temperature ratio,  $T_{\perp}/T_{\parallel}$ , with increasing  $z$ . It is expected that because the beam energy increases with  $z$ , as illustrated in Figure 5, the unstable frequencies will be functions of  $z$  in order that the cyclotron resonance velocities remain in regions of large anisotropy.

Figures 15 and 16 summarize the unstable plasma rest frame frequencies for the model distribution,  $F(z)$ . It should be noted that the

unstable frequencies are shown as a function of  $z$ . The unstable wave normal angles for a given frequency are not summarized. This is because the results obtained for the measured distributions apply to the model distribution with the main point being that for a given frequency an appreciable range of wave normal angles can be unstable.

In Figure 15, the frequencies are shown as a function of  $z$  for generation via the  $m = 0$  and  $+1$  resonances. These waves have  $k_{\parallel} < 0$ , corresponding to wave vectors directed toward the magnetosheath. A range of frequencies from about 1 to 100 Hz is unstable. This range is in good agreement with the spectrum of instabilities with  $k_{\parallel} < 0$  that are generated by the October 15, 1978, measured distribution. The fact that the model distribution is stable for  $z$  between about 50 and 100 km is consistent with the expectations outlined above. For a given value of  $z$ , the boundaries of instability correspond to the frequencies and wave normal angles that locate the resonance velocities on the boundaries of the free energy regions within  $F(z)$ . This point will not be worked out in detail because the concepts are identical to those presented in Section IV.

In Figure 16, the unstable frequencies for generation via the  $m = -1$  cyclotron resonance are shown as a function of  $z$ . These waves all have  $k_{\parallel} > 0$ , corresponding to wave vectors directed toward the magnetosheath. The range of unstable frequencies is in good agreement with the spectrum generated by the measured distributions. In addition, the unstable frequencies near the center of the transition region are consistent with the frequencies shown in Figure 14 for the



December 13, 1977, measured distributions. The increase in the unstable frequency with increasing  $z$  locates the  $m = -1$  cyclotron resonance velocity in the region of the large anisotropy. The distribution is stable for small values of  $z$  because  $T_{\perp}/T_{\parallel}$  is small and for large values of  $z$  because the Maxwellian component of  $F$  is not appreciable. As will be pointed out in the next section, this observation leads to the conclusion that the cyclotron resonant interactions are largest near the center of the transition region. In this region,  $T_{\perp}/T_{\parallel}$  is large and the Maxwellian component of  $F(z)$  is appreciable.

## VI. PROPAGATION CHARACTERISTICS OF THE GENERATED WAVES

To fully evaluate the growth of whistler mode noise in the bow shock, it is necessary to integrate the growth rate along typical ray paths. In this study, the ray paths are calculated using geometrical optics and a planar geometry for the bow shock region. The growth rate along the ray path is obtained using Equation 10 and the model electron distribution function. In this section, the results of these calculations are presented.

### A. Planar Bow Shock

To investigate the propagation of the whistler mode waves, a planar model for the bow shock region is adopted. The planar assumption is justified because the lengths along the shock normal and transverse to the shock normal that are characteristic of this study are both much less than the radius of curvature of the shock. Figure 17 illustrates the geometry. The  $\hat{z}$  axis is along the shock normal with positive  $\hat{z}$  directed from the solar wind to the magnetosheath. It should be noted that for this sign convention,  $+\hat{v}_{\parallel}$  has a component in the  $-\hat{z}$  direction. The  $\hat{x}$  axis is transverse to  $\hat{z}$ . The shock transition region extends for 100 km in the  $\hat{z}$  direction and separates the upstream solar wind from the downstream magnetosheath.

The solar wind velocity,  $\vec{v}_{sw}$ , is taken to be in the  $\hat{z}$  direction and to have the constant magnitude 400 km/s. In the model, it is assumed that the plasma flow velocity in both the solar wind and the transition region is the solar wind velocity,  $\vec{v}_{sw}$ . A more accurate description would decrease the plasma flow speed such that the product of the electron concentration and the flow speed remain constant throughout the transition region. For the electron concentration profile used in this study, the plasma flow speed would decrease linearly from 400 km/s at  $z = 0$  km to 100 km/s at  $z = 100$  km. However, because the results indicate that the important ray paths of this study are confined to small ranges of  $z$  near  $z = 50$  km, the change in the plasma flow speed over the ray paths is small. The adopted plasma flow speed, 400 km/s, is in reasonable agreement with plasma flow speeds measured in the shock transition region and illustrates most of the important propagation effects involved.

Within the shock transition region the plasma parameters are assumed to be functions only of  $z$ . The electron distribution function as a function of  $z$  is taken to be the model distribution described in Section II. The magnitude of the magnetic field,  $B(z)$ , increases linearly with  $z$ , as described by Equation 7. The shock is taken to be intermediate between the classifications parallel and perpendicular, with upstream angle between the magnetic field,  $\vec{B}$ , and  $\vec{n}$ ,  $\theta_{Bn}(z = 0)$  equal to  $45^\circ$ .

From the assumed planar geometry and the Maxwell equation  $\nabla \cdot \vec{E} = 0$ , the component of  $\vec{E}$  in the direction of the shock normal is

constant throughout the shock transition region. Therefore, the angle between  $\vec{B}$  and  $\hat{n}$  as a function of  $z$ ,  $\theta_{Bn}(z)$ , is given by the equation

$$\theta_{Bn}(z) = \cos^{-1}\left(\frac{B_0 \cos 45^\circ}{B(z)}\right) \quad (22)$$

where  $B_0$  and  $B(z)$  are given in Equation 7. In Figure 18 a magnetic field line is shown and at  $z = 70$  km,  $\theta_{Bn}(z)$  and  $B(z)$  are illustrated. Note that the field line extends for about 340 km in the  $\hat{x}$  direction.

In the planar shock model, the direction and magnitude of the magnetic field and the electron distribution function are all known as a function of  $z$ . A knowledge of these quantities enables the calculation of typical ray paths and the integration of the growth rate along the ray paths.

### B. Ray Tracing Calculations

Any position within the shock transition region where the growth rate for a given frequency and wave normal angle is positive is a source location for a whistler mode wave packet. This conclusion assumes that a background continuum of whistler mode noise with a wide range of wave normal angles is available for amplification in the shock transition region. Although the wave vector orientations of the background noise are not known, this is probably a valid assumption because Neubauer et al. [1977] have reported that a background continuum of whistler mode noise is a nearly ubiquitous feature of the solar wind.

An important question that arises is what is the subsequent trajectory and growth (or damping) of the wave packet. As stated above, in this study the ray paths emanating from the source location are calculated using the planar bow shock model and geometrical optics. Although the validity of this procedure in the turbulent shock transition region may be questionable, the results provide at least a qualitative understanding of the subsequent propagation of the generated waves.

If the turbulence in the transition region is ignored, a first-order validity criterion for ray tracing in the transition region is that the characteristic scale length for changes in the plasma parameters must be larger than the wavelength of the waves investigated. A more quantitative validity criterion for a magnetized plasma is difficult to derive [Budden, 1961]. Because the characteristic scale length is the thickness of the transition region, 100 km, in this study the ray tracing calculations are limited to waves with wavelengths less than about 25 km. This omits from the ray tracing analysis the low frequency (1 - 20 Hz) waves generated by the  $m = 0$  and  $+1$  resonances. However, this restriction is not serious because the results indicate that only the waves generated by the  $m = -1$  resonance are amplified to significant levels above the background noise.

Figures 19 and 20 illustrate the relative orientations of the magnetic field vector, the wave vector, the group velocity, and the solar wind velocity. Figure 19 applies to a wave packet propagating in the shock transition region with  $k_{\parallel} < 0$  while Figure 20 illustrates the

geometry for the case  $k_{\parallel} > 0$ . The unstable wave vectors lie on a cone with axis along the magnetic field direction and with half angle equal to the wave normal angle,  $\theta$ . Of this set of wave vectors, two extreme initial orientations are considered in this study. These wave vectors lie in the plane of Figures 18, 19 and 20 and are distinguished by the angle  $\phi$  with the  $\phi = 0^\circ$  direction defined to be towards the solar wind. The  $\phi = 180^\circ$  direction is the wave vector that lies on the unstable cone of wave vectors and is  $180^\circ$  in azimuth from the  $\phi = 0^\circ$  orientation.

For a given wave frequency and wave normal angle the direction of the group velocity,  $\vec{v}_g$ , defines the direction of the ray path in the plasma rest frame. To obtain the ray paths in the frame of reference of the shock, the plasma convection must be taken into account. Consequently, in the shock frame of reference the direction of the ray path at a given point is the direction of the vector  $\vec{v}_g + \vec{v}_{sw}$  at that point. This is because, as discussed previously,  $\vec{v}_{sw}$  is taken to be the plasma flow velocity in both the solar wind and transition region. In Figures 19 and 20, the solar wind velocity is shown at the head of the group velocity. The relative magnitudes of  $\vec{v}_g$  and  $\vec{v}_{sw}$  depicted in Figures 19 and 20 are typical of this study.

The magnitude and direction of the group velocity are calculated using the expression for the index of refraction of the whistler mode. For the frequencies of interest in this study, a good approximation for the index of refraction is Equation 15.

$$n = \frac{ck}{\omega_r} = \frac{\omega_p}{\omega_r^{1/2} (\omega_g \cos \theta - \omega_r)^{1/2}} \quad (15)$$

In Equation 15,  $\omega_r$  is the real frequency of the wave,  $\omega_p$  is the electron plasma frequency,  $\omega_g$  is the electron gyrofrequency, and  $\theta$  is the wave normal angle. From this equation the magnitude of the group velocity is found to be

$$|\vec{v}_g| = \frac{\partial \omega_r}{\partial k} = \frac{2\omega_r^{1/2} c (\omega_g \cos \theta - \omega_r)^{3/2}}{\omega_p \omega_g \cos \theta} \quad (23)$$

The angle between  $\vec{v}_g$  and  $\vec{k}$  is denoted by  $\alpha$  and is shown by Stix [1962] to be equal to

$$\alpha = \tan^{-1} \left( -\frac{1}{n} \frac{\partial n}{\partial \theta} \right) \quad (24)$$

It is shown in many texts (e.g., see Stix [1962]) that this equation is equivalent to the statement that the group velocity is always perpendicular to the index of refraction surface. In terms of  $\alpha$ , the angle between  $\vec{v}_g$  and  $\vec{B}$ ,  $\psi$ , is given by the equation

$$\psi = \theta + \alpha = \theta + \tan^{-1} \left( \frac{-\sin \theta}{2(\cos \theta - \omega/\omega_g)} \right) \quad (25)$$

The angle  $\psi$  is indicated in Figures 19 and 20. When the condition  $|\omega_r| \ll |\omega_g \cos \theta|$  is satisfied,  $\psi$  is confined to magnitudes less than about  $20^\circ$  [Stix, 1962].

To facilitate the understanding of the ray tracing procedure, the steps followed in a typical calculation will be listed individually.

- 1.) For a chosen frequency and initial wave normal angle, identify the values of  $z$  for which the growth rate,  $\omega_i(z)$ , is positive.
- 2.) For waves with  $k_{\parallel} > 0$ , begin the calculations at the largest value of  $z$  for which  $\omega_i(z)$  is positive and for waves with  $k_{\parallel} < 0$ , begin at the smallest value of  $z$  for which  $\omega_i(z)$  is positive. In the majority of cases, these source locations will lead to maximum growth of the initial signal because the wave packet will spend the maximum time in the growth region.
- 3.) Calculate  $\vec{v}_g$  using Equations 23 through 25.
- 4.) To obtain the ray path in the shock frame, add to  $\vec{v}_g$  the plasma flow velocity. In this study, the plasma flow velocity is taken to be  $\vec{v}_{sw} = 400 \text{ km/s } \hat{z}$  in both the solar wind and transition region.
- 5.) Advance the wave packet along  $\vec{v}_g + \vec{v}_{sw}$  for a fixed increment in  $z$ . The increment in  $z$ ,  $\Delta z$ , of 4 km is used in this study.
- 6.) Calculate the amplification along the segment of the ray path connecting  $z$  and  $z + \Delta z$ . Denoting the length of the segment by  $\Delta s$ , the amplification along the segment,  $\Delta \Gamma$ , is approximated by



$$\Delta\Gamma(z) = \frac{\omega_i(z) \Delta s}{|\vec{v}_g + \vec{v}_{sw}|}$$

Over this segment of the ray path, the fields are amplified by the factor  $e^{\Delta\Gamma}$ .

- 7.) At the position  $z + \Delta z$ , calculate the wave normal angle of the wave packet using the condition that the  $\hat{x}$  component of the index of refraction vector remains constant along the ray path. This condition is Snell's law and is a consequence of the planar geometry.
- 8.) Repeat steps 3 through 7 throughout the growth region.
- 9.) Calculate the net amplification,  $\Gamma$ , in the growth region by adding together the values of  $\Delta\Gamma$  for each segment of the ray path.

Figure 21 summarizes the results of the ray tracing calculations. Note that the figure is compressed by a factor of 10 in the  $\hat{x}$  direction. In Figure 21 a magnetic field line is illustrated as are several ray paths. The ray paths are labeled using wave frequency, initial wave normal angle and initial value of  $\phi$  in the format  $(\omega_r/2\pi, \theta_0, \phi)$ . A  $\phi$  value for  $\theta_0 = 0^\circ$  is not applicable and so is omitted from the ray path labels. The ray paths terminate when the growth rate becomes negative. The net amplification along the ray path,  $\Gamma$ , defined by point 9 above is given at the heads of the arrows denoting the ray path. This

number must be exponentiated to obtain the total amplification of the initial signal.

In this study, three initial wave vector directions are analyzed. They are  $\theta_0 = 0^\circ$ ,  $\theta_0 = 45^\circ$  with  $\phi = 0^\circ$ , and  $\theta_0 = 45^\circ$  with  $\phi = 180^\circ$ . These initial wave vector directions illustrate all of the important ray paths in the transition region. The results for generation via the  $m = 0$  and  $+1$  resonances and for generation via the  $m = -1$  resonance are discussed separately.

In the lower left corner of Figure 21, ray paths for generation via the  $m = 0$  and  $+1$  resonances are shown. The frequency  $\omega_r/2\pi = 50$  Hz has associated wavelengths always less than 25 km and serves to illustrate the important propagation characteristics for the case  $k_{\parallel} < 0$ . Two initial wave vector orientations,  $\theta_0 = 45^\circ$  with  $\phi = 0^\circ$  and  $\theta_0 = 45^\circ$  with  $\phi = 180^\circ$  are analyzed. The case  $\theta_0 = 0^\circ$  is omitted from the calculations because the growth rate is always negative for  $k_{\parallel} < 0$  and  $\theta_0 = 0^\circ$ . This is because the  $m = 0$  and  $+1$  contributions to  $\omega_i$  are zero at  $0^\circ$ , as explained in Section IV.

As illustrated in Figure 21, the ray paths for the frequency  $\omega_r/2\pi = 50$  Hz and the two initial wave normal angles are directed toward the magnetosheath. This is due to the fact that both the group velocity and the solar wind velocity are directed towards the magnetosheath, as shown in Figure 19. The important point for the case  $k_{\parallel} < 0$  is that the values obtained for  $\Gamma$  are small. The values of 0.4 and 0.5 given in Figure 21 are typical for all wave packets with  $k_{\parallel} < 0$ .

The small amplification arises because the time spent in the growth region and the growth rates in the region are small. The convection of the plasma toward the magnetosheath at the solar wind speed, 400 km/s, also contributes to the small amplification. However, in contrast to the case  $k_{\parallel} > 0$ , the solar wind convection effect is not large because the group velocity is directed predominantly toward the magnetosheath with a magnitude typically 3 to 5 times as large as the plasma flow speed.

For values of  $z$  greater than about 50 km, the growth rate is small and negative. A period of small growth followed by a period of small damping is typical for all wave packets generated by the  $m = 0$  and  $+1$  resonances.

Originating on the right-hand side of Figure 21 are the ray paths for generation via the  $m = -1$  resonance. The three frequencies treated,  $\omega_r/2\pi = 70, 90$ , and 110 Hz, together with the three initial wave vector orientations, illustrate all of the important propagation characteristics for the case  $k_{\parallel} > 0$ .

As is clear from an inspection of Figure 21, the amplification of the waves with  $k_{\parallel} > 0$  can be large. The values of  $\Gamma$  obtained range from .3 to 93. The largest amplification occurs for waves with  $\theta_0 = 45^\circ$  and  $\phi = 180^\circ$ . This is because for these wave packets the solar wind convection effect causes  $\vec{v}_g + \vec{v}_{sw}$  to be directed predominantly transverse to  $\hat{z}$  resulting in the wave packet spending a large time in the growth region. A good example of this effect is the case  $\omega_r/2\pi = 110$  Hz for which the ray path is directed toward the

magnetosheath. An additional contributor to the large amplification is that the growth rates for the case  $k_{\parallel} > 0$  are large. However, as mentioned in Section III, the ratios  $\omega_i/\omega_T$  used in the calculations are never allowed to be larger than .5.

The three frequencies analyzed are generated near the center of the shock transition region where the cyclotron interactions are strongest. For frequencies lower than 70 Hz or higher than 110 Hz the growth rates are small. Therefore, the growth rate integrated along the ray path is small. Typical values of  $\Gamma$  for the lower and higher frequencies would be between about one-tenth and one-hundredth of the values given in Figure 21. In all cases with  $k_{\parallel} > 0$ , the period of large growth is followed by a period of equally large damping. Because of this fact and because the ray paths are confined to small ranges of  $z$  near the center of the transition region, the waves generated by the  $m = -1$  resonance are not expected to travel into the solar wind.

The results of the ray tracing calculations are summarized as follows:

- 1.) The waves generated by the  $m = 0$  and  $+1$  resonances follow ray paths that are directed towards the magnetosheath. The wave packet traverses the transition region quickly, experiencing a period of small growth followed by a period of small damping. Because the background whistler mode noise is not significantly amplified, large amplitude wave packets with  $k_{\parallel} < 0$  are not expected to reach the magnetosheath.

- 2.) Many of the waves generated by the  $m = -1$  resonance achieve large amplitudes. The instabilities with largest amplitude lie in the frequency range from about 70 to 110 Hz and are generated near the center of the shock transition region. The largest growth occurs for oblique wave normal angles with ray paths primarily transverse to  $\hat{z}$ . In all cases, the large growth is followed by large damping and so the waves are not expected to escape the transition region.

## VII. DISCUSSION

The integrated growth calculations presented in the previous section suggest that the electron beams present in the bow shock generate whistler mode waves with large amplification factors and that the waves are absorbed by the shock transition region. Before comparing the predictions of the study with observations of whistler mode noise at the shock, it is desirable to discuss to what degree these conclusions depend on two important assumptions. These assumptions are that the electron velocity distribution as a function of shock penetration is the model distribution,  $F(z)$ , and that the upstream angle between the magnetic field and the shock normal,  $\theta_{Bn}(z = 0)$ , is  $45^\circ$ .

The electron velocity distribution,  $F(z)$ , plays an important role in the integrated growth calculations because  $F(z)$ , together with the growth rate formula given by Equation 10, determines the size of the growth region and the magnitudes of the growth rates. By varying the free parameter models used to define  $F(z)$ , both the size of the growth region and the magnitudes of the growth rates can be increased or decreased. However, because the adopted model agrees with observation in the transition region and because  $F(z)$  is unstable to a large spectrum of whistler mode waves, some with large integrated growth, this point is not pursued.

The important point that the adopted model  $F(z)$  neglects is the possibility that the solar wind and magnetosheath velocity distributions may be unstable to whistler mode waves. Sentman et al. [1983] reported recently that some foreshock electron velocity distributions are unstable to approximately 1 Hz whistler mode waves. In addition, a few of the magnetosheath electron distributions in Feldman et al. [1983] possess velocity space anisotropies that, although yet unproven, appear to be unstable to whistler mode waves. This suggests that the solar wind and magnetosheath boundaries of the shock transition region can be source regions for whistler mode waves. The conclusion that the waves discussed in this study are confined to the shock transition region is due in part to the adopted isotropic distributions at the solar wind and magnetosheath. If the waves encounter regions near the solar wind or magnetosheath that either amplify or are marginally stable to whistler mode instabilities, they may escape the transition region.

To investigate the effect of the chosen value for  $\theta_{Bn}(z = 0)$  of  $45^\circ$ , the limiting cases of a parallel shock ( $\theta_{Bn}(z = 0)$  equal to  $0^\circ$ ) and a perpendicular shock ( $\theta_{Bn}(z = 0)$  equal to  $90^\circ$ ) are discussed. For a parallel shock  $\theta_{Bn}(z)$  will range from  $0^\circ$  at  $z = 0$  km to about  $75^\circ$  at  $z = 100$  km. For  $z$  greater than about 14 km,  $\theta_{Bn}(z)$  is greater than  $45^\circ$ . These calculations assume that the component of  $\vec{B}$  in the direction of the shock normal is constant and that the magnitude of  $B$  increases with  $z$  as in Equation 7. Because  $\theta_{Bn}(z)$  increases rapidly with  $z$  and attains values greater than  $45^\circ$  throughout most of the

transition region, the  $\theta_{Bn}(z)$  profiles in the shock transition region are similar for both  $\theta_{Bn}(z = 0)$  equal to  $0^\circ$  and  $45^\circ$ . Consequently, the ray paths and integrated growths for these two models should be similar.

As  $\theta_{Bn}(z = 0)$  increases toward  $90^\circ$ , the component of  $\vec{B}$  in the direction of  $\hat{n}$  approaches zero. For these shocks,  $\theta_{Bn}(z)$  is near  $90^\circ$  for all values of  $z$ . Because the group velocity of the waves is usually within about  $20^\circ$  of  $\vec{B}$ , many waves can have ray paths that are directed transverse to the shock normal. These waves will spend long periods of time in the growth region and thereby grow to large amplitudes.

An additional effect for perpendicular or nearly perpendicular shocks is that for these shocks the component of the electric field within the transition region that is in the direction of  $\vec{B}$  is expected to be small. Consequently, it is possible that the plasma will be convected through the transition region before an appreciable electron beam is produced.

The above discussion suggests that the propagation characteristics of the generated whistler mode waves will be similar to the results presented in this study if  $\theta_{Bn}(z = 0)$  is less than or equal to about  $45^\circ$ . As  $\theta_{Bn}(z = 0)$  increases towards  $90^\circ$ , two competing effects arise. The first is that the number of wave packets travelling transverse to the shock normal increases. These waves are expected to attain large amplitudes. The second is due to the decrease in the component of the



transition region electric field that is in the direction of  $\vec{B}$ . This decrease hinders the production of the field-aligned electron beam. For these reasons, the results of this study do not apply to perpendicular or nearly perpendicular shocks.

It is desirable to compare the predictions of this study with the observations of whistler mode noise at the bow shock shown in Figure 1. Because  $\theta_{Bn}(z = 0)$  is equal to  $65^\circ$  for this shock, the results presented in Section VI should apply. Two comparisons can be made. The predicted frequencies of the instabilities can be compared with observation and the measured amplitudes of the waves can be compared with the integrated growth calculations. However, because the initial angular distributions of the observed waves are not known, the predicted wave vector directions cannot be compared with observation.

As was discussed in the last section, the instabilities generated by the  $m = -1$  resonance have the largest integrated growth rates. For this reason, the unstable frequencies for generation via this resonance should be compared to the frequencies for the large amplitude noise shown in Figure 1. In Figure 1, the range in frequency over which the whistler mode noise is observed is about 5.6 Hz to 100.0 Hz. From the previous section, the predicted plasma rest frame frequencies for the large amplitude waves generated via the  $m = -1$  resonance range from about 70 Hz to 110 Hz. This leads to the conclusion that the two frequency ranges are in rough agreement.

This agreement is improved if the Doppler-shift caused by the relative motion of the satellite and the plasma is taken into account.

Because the wave vectors of many of the waves generated by the  $m = -1$  resonance are directed into the solar wind flow, the Doppler-effect for these waves results in a measured frequency that is lower than the plasma rest frame frequency. When the wave vector has a component in the direction of the solar wind flow, the measured frequency will be higher than the plasma rest frame frequency. It is not necessary to work out the Doppler-shift for all rays because a typical calculation will illustrate the magnitude of the effect involved.

The Doppler-shifted frequency of the wave can be calculated using the equation

$$\omega = \omega' + \vec{k} \cdot \vec{v}_{sw} \quad (26)$$

where  $\omega'$  is the rest frame frequency,  $\vec{k}$  is the rest frame wave vector, and  $\omega$  is the Doppler-shifted frequency. The measured frequency will be lower than  $\omega'$  if  $\vec{k} \cdot \vec{v}_{sw}$  is less than zero and greater than  $\omega'$  if  $\vec{k} \cdot \vec{v}_{sw}$  is greater than zero.

To illustrate the effect, consider the rest frame frequency 100 Hz and the two wave vector orientations  $\theta = 45^\circ$  with  $\phi = 0^\circ$  and  $\theta = 45^\circ$  with  $\phi = 180^\circ$ . From the results presented in Figure 21, these wave packets exist near  $z = 50$  km and have large integrated growth rates. Employing Equation 26 to calculate the measured frequency for the two wave vector orientations, it is found that for the  $\phi = 0^\circ$  orientation

of  $\vec{k}$  the frequency is downshifted to about 78 Hz and for the  $\phi = 180^\circ$  orientation of  $\vec{k}$  the frequency is upshifted to about 112 Hz.

This effect can be increased dramatically if highly oblique wave normal angles are considered. This is because the magnitude of the wave vector,  $|\vec{k}|$ , goes to infinity as the wave normal angle approaches the resonance cone angle,  $\theta_{\text{Res}} = \cos^{-1}(\omega_r/\omega_g)$ . However, because the hot plasma effects on the whistler dispersion relation may be important near the resonance cone, this possibility will not be discussed here.

From the above calculations it is concluded that the agreement between the predicted and measured frequency ranges is improved if the Doppler effect is taken into account. However, because the approximately 20% downshift in frequency is typical for the large amplitude waves with wave vector orientations  $\theta_0 = 45^\circ$  and  $\phi = 0^\circ$ , only if highly oblique wave normal angles are considered is it possible to downshift the predicted frequencies to the lowest frequencies measured.

It is also important to investigate whether or not the instabilities of this study can attain the large amplitudes of the shock associated whistler mode noise shown in Figure 1. From Neubauer et al. [1977], it is found that typical spectral densities of whistler mode noise in the solar wind near 1 AU are  $10^{-3}$  to  $10^{-2}$  gammas/(Hz) $^{1/2}$  for the frequency 7 Hz and  $10^{-4}$  gammas/(Hz) $^{1/2}$  for the frequency 70 Hz. These amplitudes for the background noise are to be compared to amplitudes of whistler mode noise in the shock transition region. An estimate of the amplification required can be obtained from the ISEE-1

plasma wave receiver on December 13, 1977. Figure 1 illustrates that at 17:35:15.0 UT on this day ISEE-1 is in the shock transition region and large amplitude whistler mode noise is present. At this time, spectral densities for the noise are about  $1 \text{ gamma}/(\text{Hz})^{1/2}$  at 7 Hz and  $10^{-2} \text{ gamma}/(\text{Hz})^{1/2}$  at 70 Hz.

From these results, it is concluded that the total amplification of the background noise must be a factor of  $10^2$  or  $10^3$ . This corresponds to a range in  $\Gamma$  from about 5 to 7. It is clear from an inspection of Figure 21 that many of the generated waves have amplification factors large enough to give rise to the large amplitude whistler mode noise at the shock. This noise is expected to have maximum intensity near the center of the shock transition region or magnetic ramp. This is in agreement with Figure 1 where the noise has maximum intensity near the center of the shock transition region at about 17:35.13.0 UT.

## VII. CONCLUSION

This study demonstrates that the electron beams measured by the ISEE fast plasma experiments in the transition region of the bow shock generate whistler mode instabilities via electromagnetic Landau and cyclotron resonance. Many of the generated wave packets can attain the large amplitudes typical of whistler mode waves at the shock. The predicted frequencies of the waves and the observed frequencies of whistler mode noise at the shock are in fairly good agreement.

The study does not account for the low frequency large amplitude noise observed in the shock transition region. In addition, the results of the study do not provide a direct explanation for the origin of the whistler mode noise in the solar wind and magnetosheath boundary regions of the shock. It is plausible that these discrepancies are a consequence of the idealized models adopted and that in actuality most of the whistler mode noise observed at the shock is generated in the transition region and propagates into the upstream solar wind and downstream magnetosheath.

Table 1

Parameters That Specify the Measured Velocity Distributions

DATE AND TIME (UT)	$C_1$ (Arbitrary) Units	$C_2$ (Arbitrary) Units	$v_1$ ( $\times 10^8$ cm/s)	$v_2$	$v_3$	P	R	$T_L$ (°K)	$T_H$ (°K)
10/15/78 18:21:02.0	$6.14 \times 10^7$	$6.00 \times 10^7$	0.0	2.600	1.970	3.29	2.29	$4.00 \times 10^5$	$3.60 \times 10^4$
12/13/77 17:34:55.7	$2.10 \times 10^7$	$1.20 \times 10^7$	0.0	3.650	3.255	3.43	2.43	$2.70 \times 10^5$	$2.00 \times 10^4$
12/13/77 17:34:58.5	$8.05 \times 10^6$	$7.10 \times 10^6$	.277	5.250	5.363	4.26	3.00	$2.60 \times 10^5$	$2.40 \times 10^4$

Table 2

Shock Parameters For the Measured Distributions

DATE AND TIME (UT)	$\theta_{Bn}$ (Degrees)	Magnetic Local Time (Hours)	Radial Distance ( $R_E$ )	$\omega_p/2\pi$ (kHz)	$\omega_g/2\pi$ (Hz)
10/15/78 18:21:02.0	35	12.6	14.3	20	110
12/13/77 17:34:55.7	65	8.2	16.8	20	315
12/13/77 17:34:58.5	65	8.2	16.8	20	315

Figure 1

This figure illustrates typical observations of whistler mode noise at the bow shock. The figure depicts data obtained with the ISEE-1 plasma wave experiment and the magnetic field experiment. The top panel shows the wave magnetic fields in ten frequency channels while the bottom panel illustrates the magnetometer data. The magnetic ramp defining the shock transition region is clearly visible as is the large amplitude whistler mode noise at the shock. The noise is most intense within the shock transition region and extends into the upstream solar wind and downstream magnetosheath.



A-683-389-1

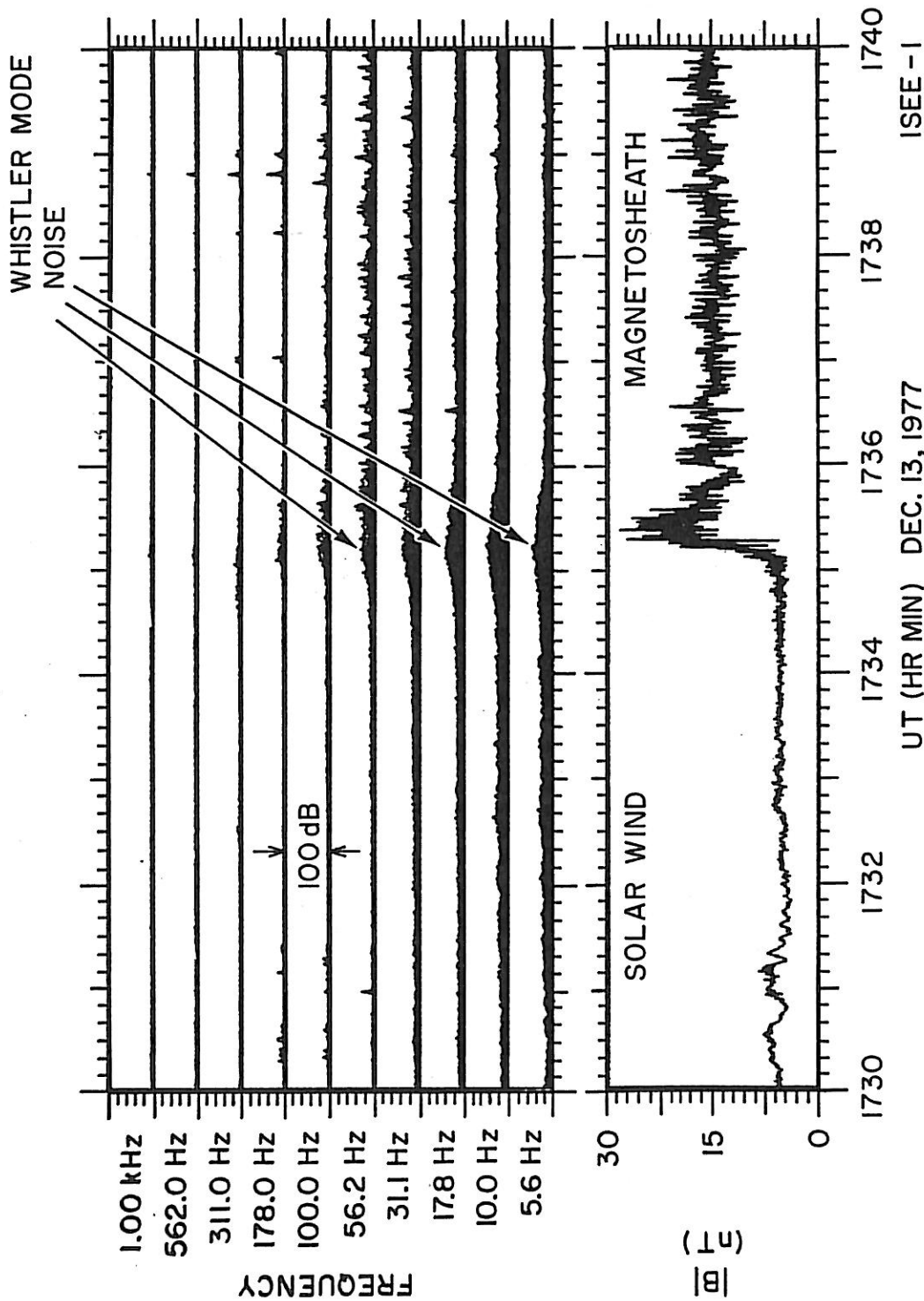


Figure 1

Figure 2

This figure, reproduced from Feldman et al. [1982], shows parallel slices of electron distribution function data measured by the ISEE 2 fast plasma experiment. As the satellite moves from the solar wind into the magnetosheath, field-aligned electron beams are observed.

ISEE 2  $\Phi = -60^\circ$  13 DEC 1977

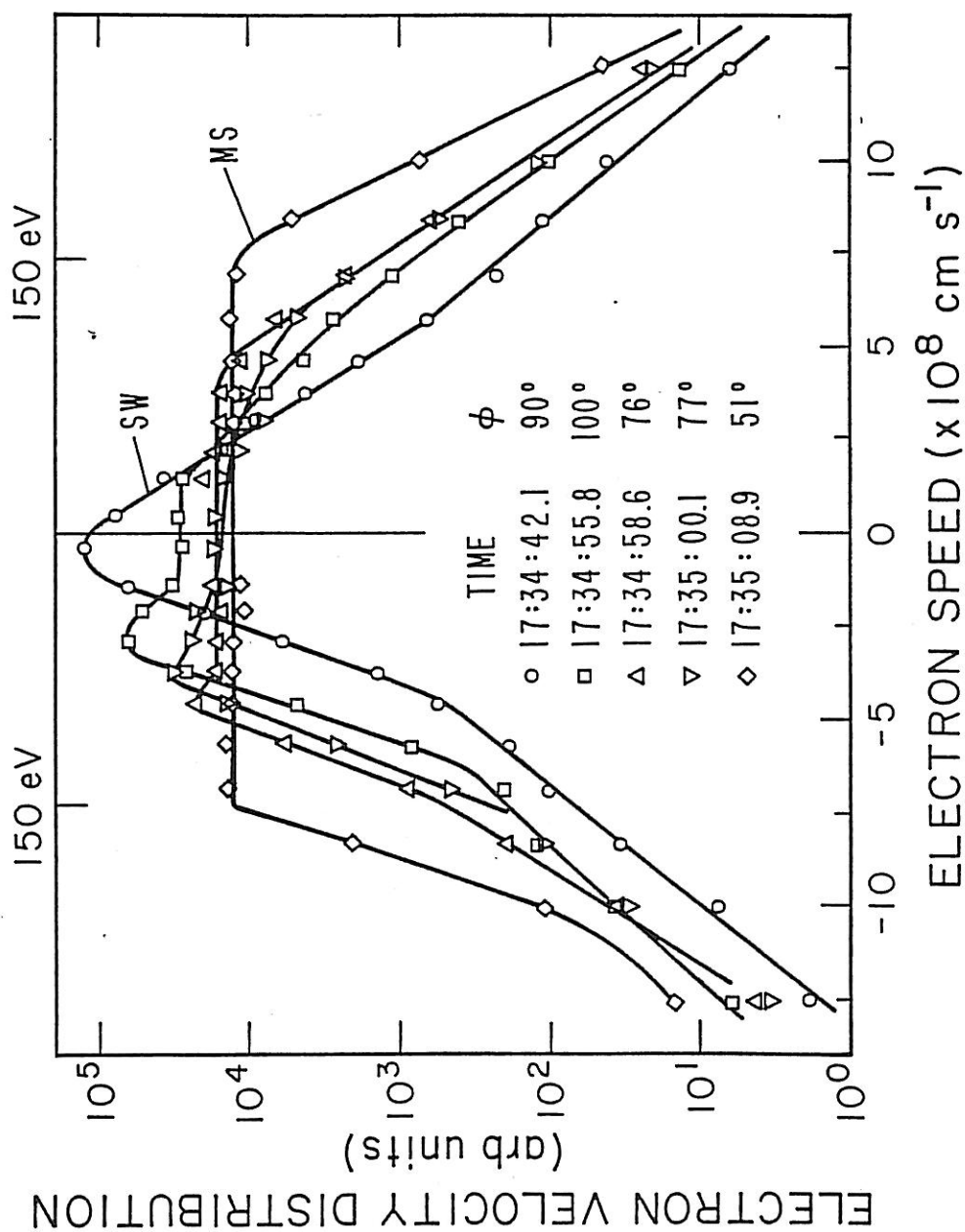


Figure 2

Figure 3

This figure depicts contour plots of the logarithm of the analytic fits to the fast plasma experimental electron distribution function data analyzed in this study. These distribution functions were measured within the transition region of Earth's bow shock. A modified Lorentzian models the flat-topped component of the electron distribution and a convected Maxwellian with a  $T_{\perp} > T_{\parallel}$  anisotropy models the field-aligned electron beam.

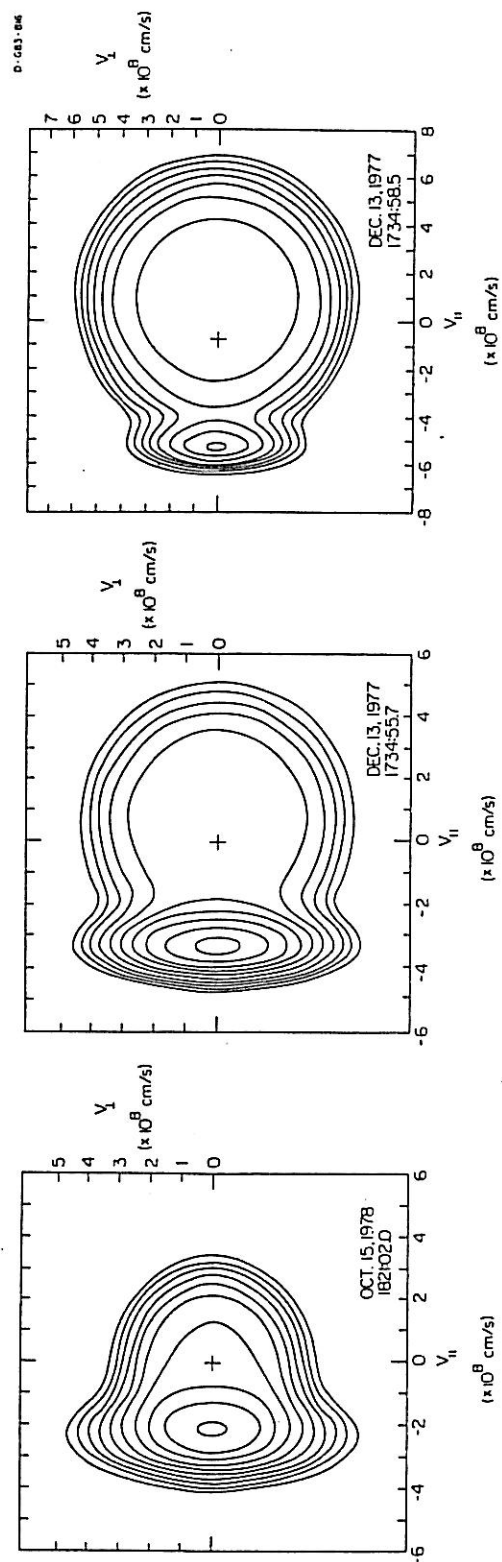


Figure 3

Figure 4

This figure depicts the dependence on shock penetration of the convection speed of the Maxwellian component of the model distribution. The convection speed is zero at the solar wind and increases to about  $6 \times 10^8$  cm/s at the magnetosheath. The increase in the convection speed is produced by a constant electric field within the transition region. The potential drop across the shock is taken to be 100 volts.

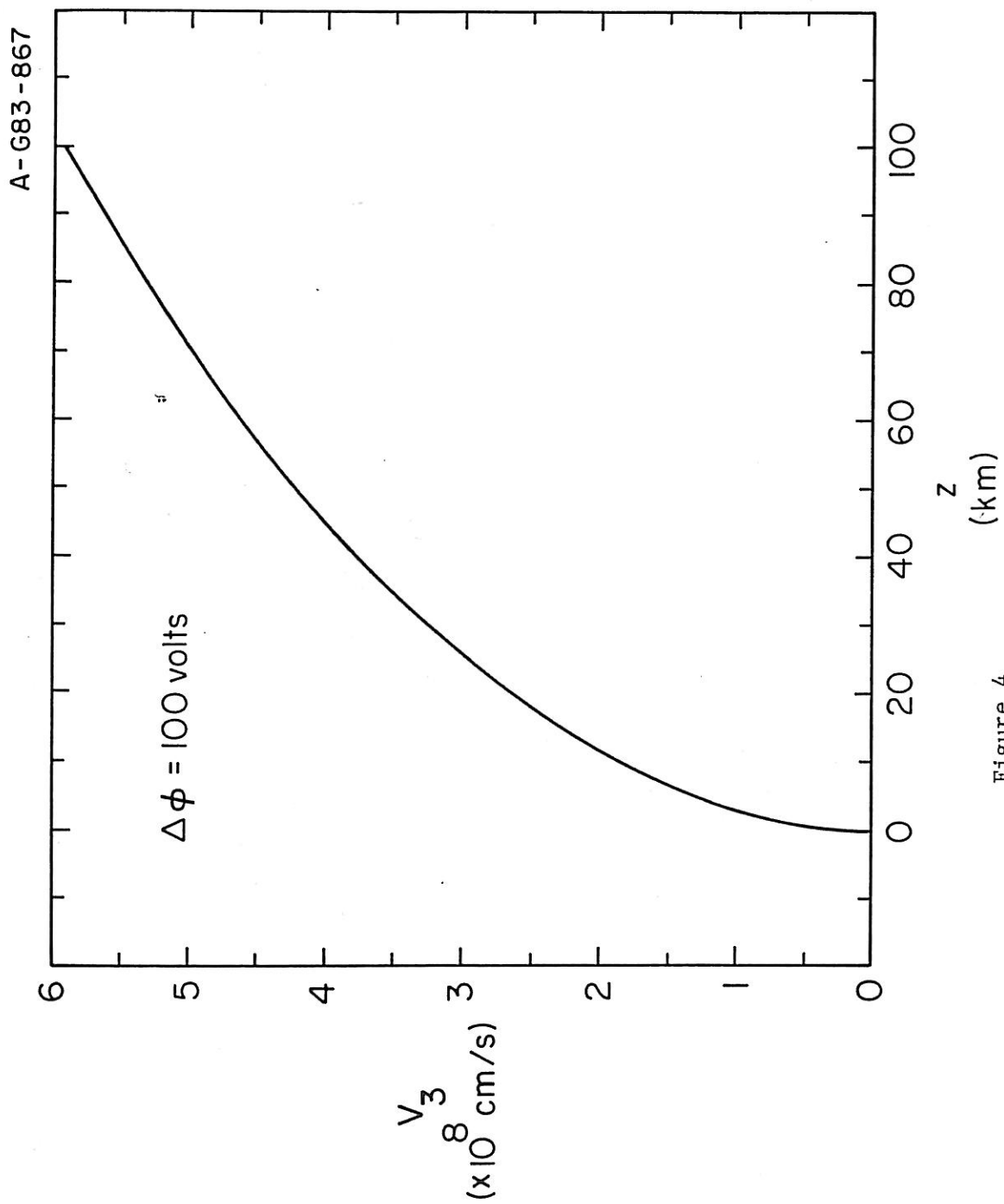


Figure 4

Figure 5

This figure depicts the increase in the electron plasma frequency with increasing shock penetration. This increase reflects the increase in the electron concentration measured by the fast plasma experiment on December 13, 1977. The plasma frequency increases from about 14 kHz at the solar wind to about 28 kHz at the magnetosheath. This variation with  $z$  of the plasma frequency is used in many calculations of this study.



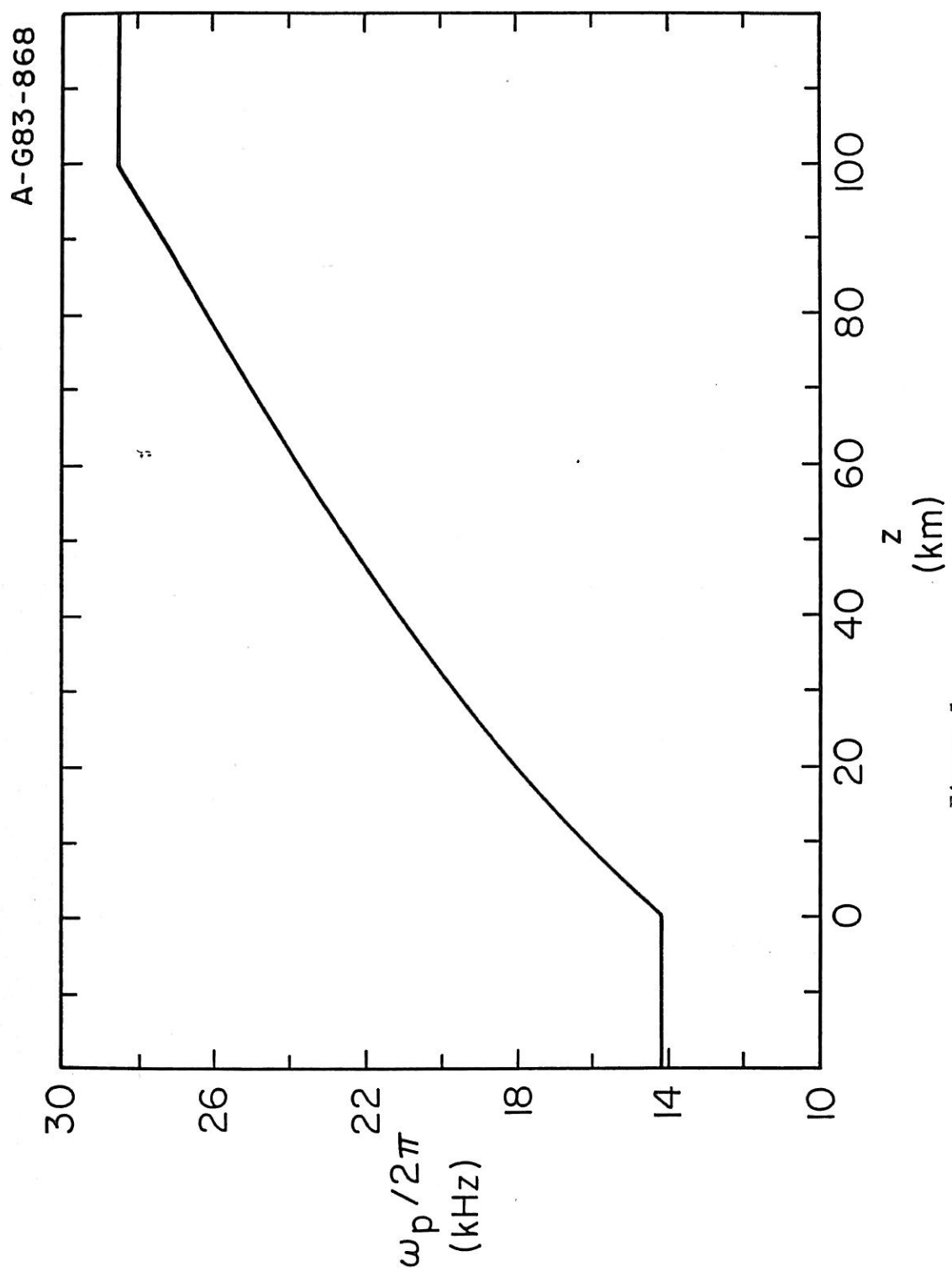


Figure 5

Figure 6

This figure depicts the increase in the electron gyrofrequency with increasing shock penetration. This increase reflects the increase in the magnetic field magnitude measured by the magnetic field experiment on December 13, 1977. The gyrofrequency increases from about 140 Hz at the solar wind to about 560 Hz at the magnetosheath. This variation with  $z$  of the gyrofrequency is used in many calculations of this study.

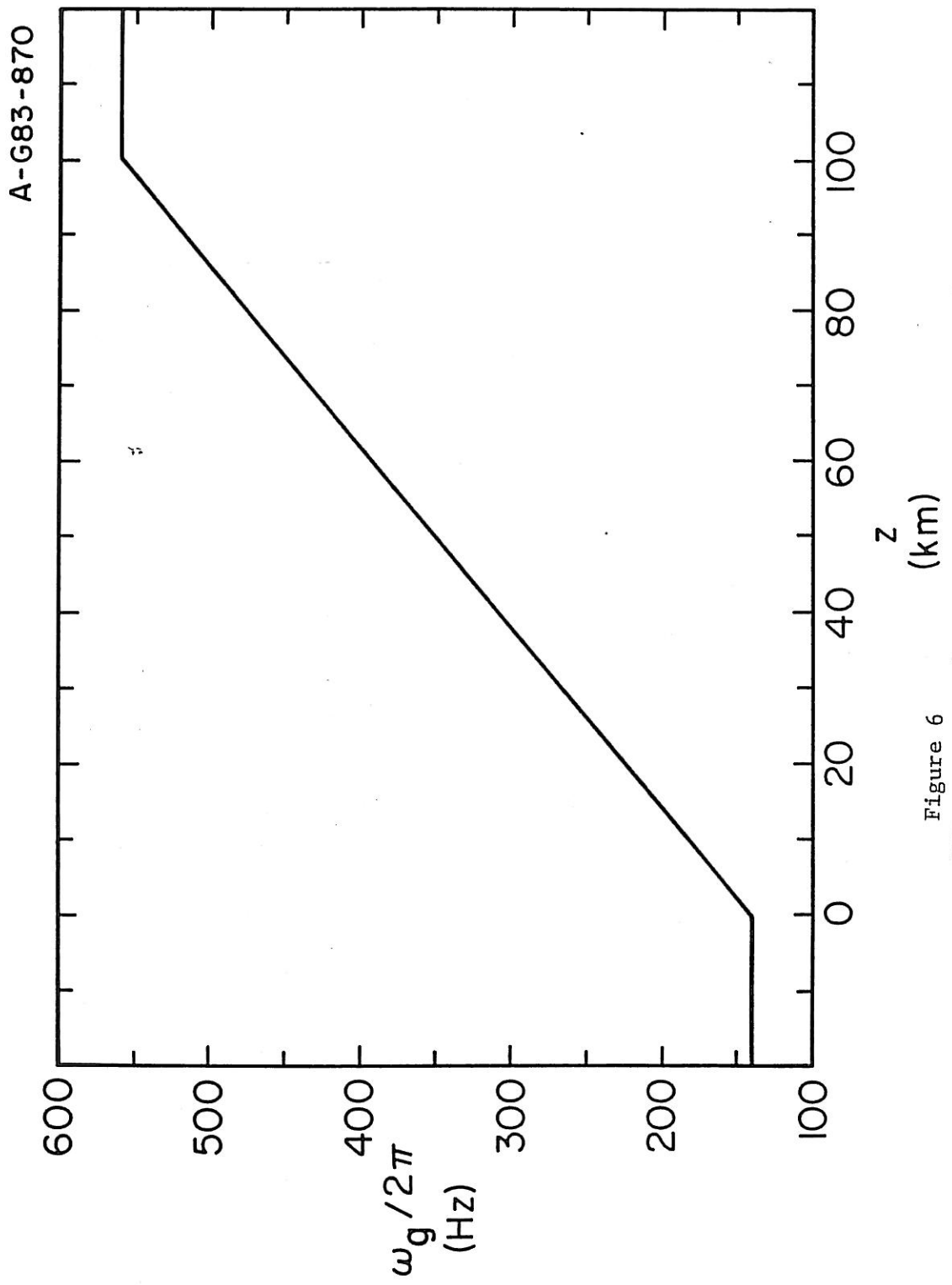


Figure 6

Figure 7

This figure depicts the variation with shock penetration of the perpendicular and parallel beam temperatures. The increase in the perpendicular temperature is consistent with conservation of the first adiabatic invariant of the electrons as the electrons move from the solar wind to the magnetosheath. The parallel temperature decreases from the solar wind value of  $1.5 \times 10^5 \text{°K}$  to  $2 \times 10^4 \text{°K}$  at the center of the transition region. This decrease is consistent with the December 13, 1977, measured distributions and is, by and large, attributable to the Maxwellian in the parallel direction. For  $z$  larger than 50 km, the parallel temperature is held constant.

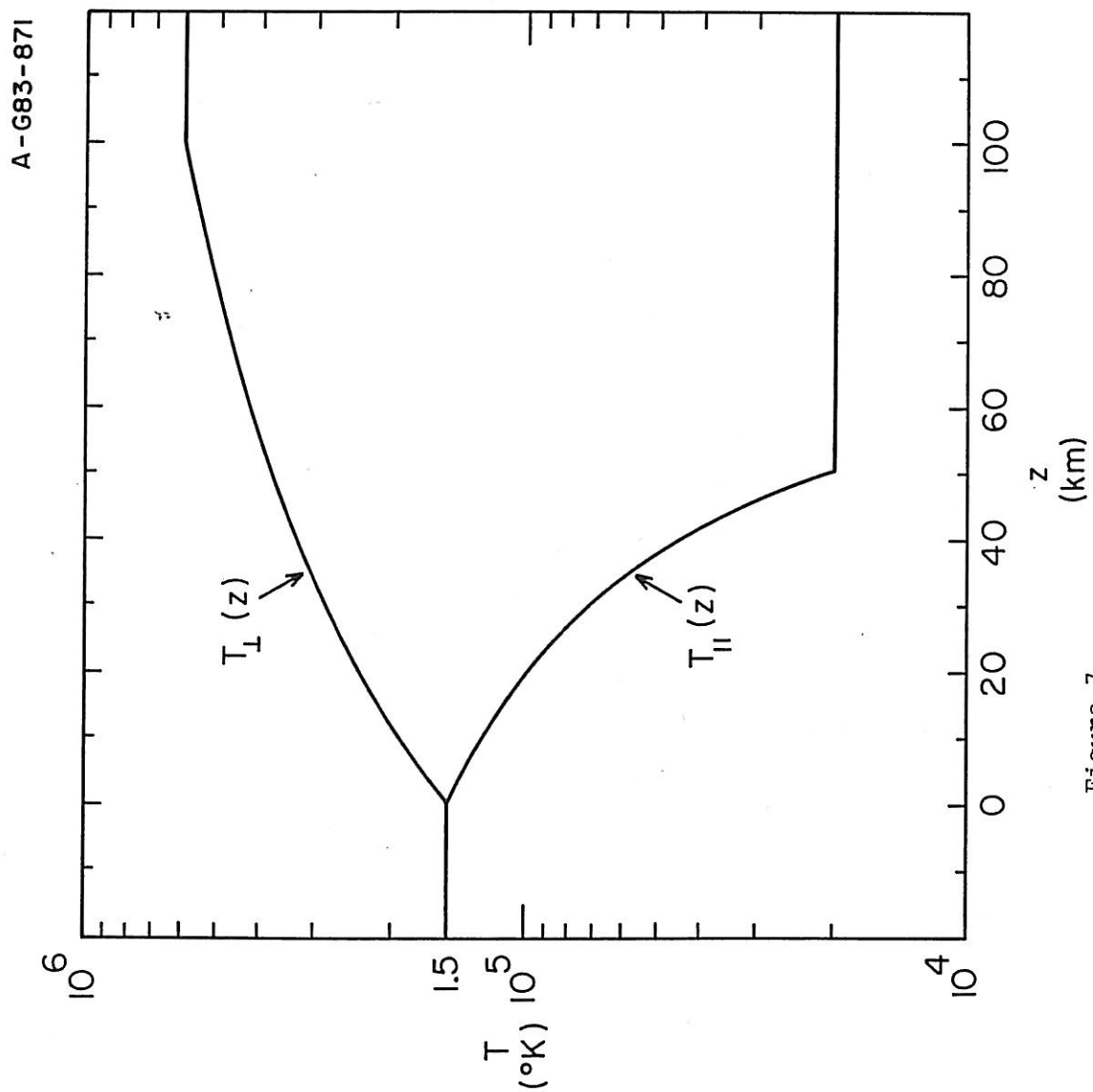


Figure 7

Figure 8

This figure depicts contour plots of the logarithm of the model electron velocity distribution as a function of shock penetration,  $z$ . The distribution evolves from a relatively cool Maxwellian at the solar wind ( $z = 0$  km) to a relatively hot modified Lorentzian at the magnetosheath ( $z = 100$  km). As the beam energy increases, the anisotropy ratio,  $T_{\perp}/T_{\parallel}$ , increases as does the modified Lorentzian component of the model distribution.

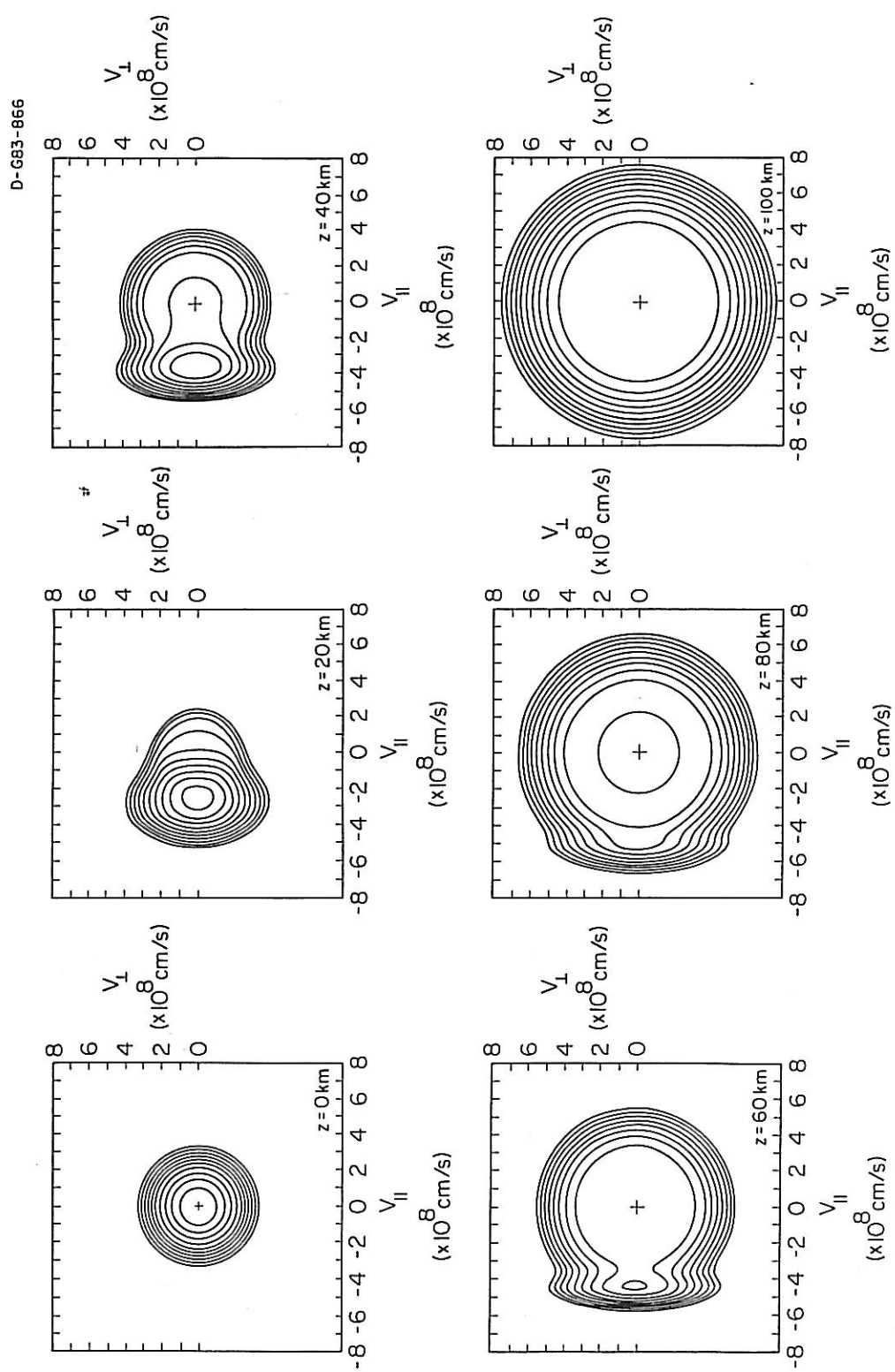


Figure 8

Figure 9

The left column of this figure presents a sample of the growth rates obtained for the electron distribution function measured on December 13, 1977, at 17:35:55.7 UT. Plotted is the ratio of the total growth rate to real frequency. The growth rate is positive because the positive contribution of the  $m = -1$  resonance is larger than the negative contributions of the  $m = 0$  and  $+1$  resonances. The right column of this figure depicts the  $m = -1$  cyclotron resonance velocity as a function of wave normal angle for the two frequencies of interest.



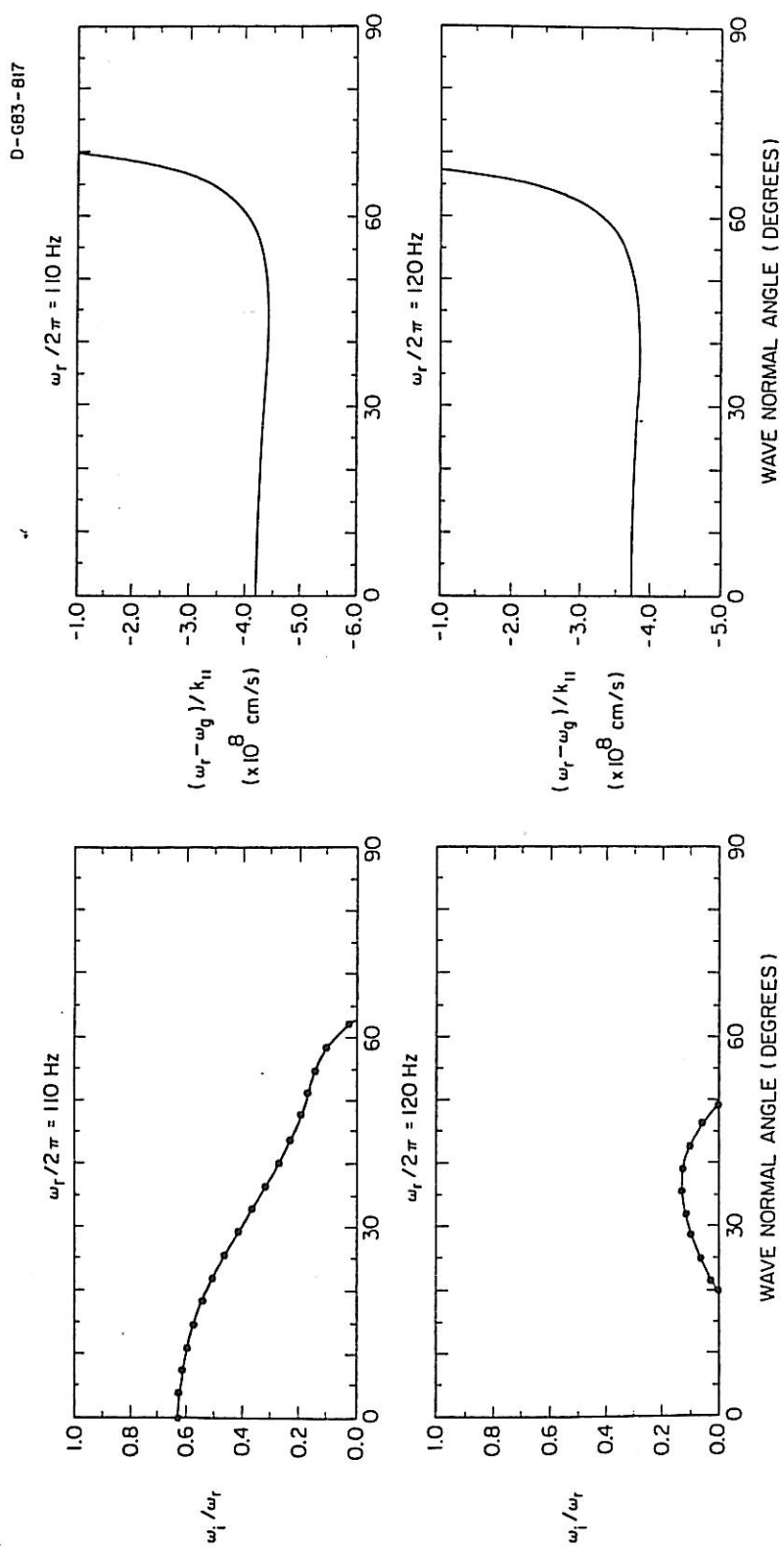


Figure 9

Figure 10

In this figure, the range in the  $m = -1$  cyclotron resonance velocity corresponding to instability for  $\omega_r/2\pi = 110$  Hz, as obtained from Figure 2, is overlaid on a contour plot of the electron distribution function measured on December 13, 1977, at 17:34:55.7. The  $m = -1$  cyclotron resonance velocities lie in regions of large anisotropy,  $\frac{\partial F}{\partial \alpha} < 0$ .

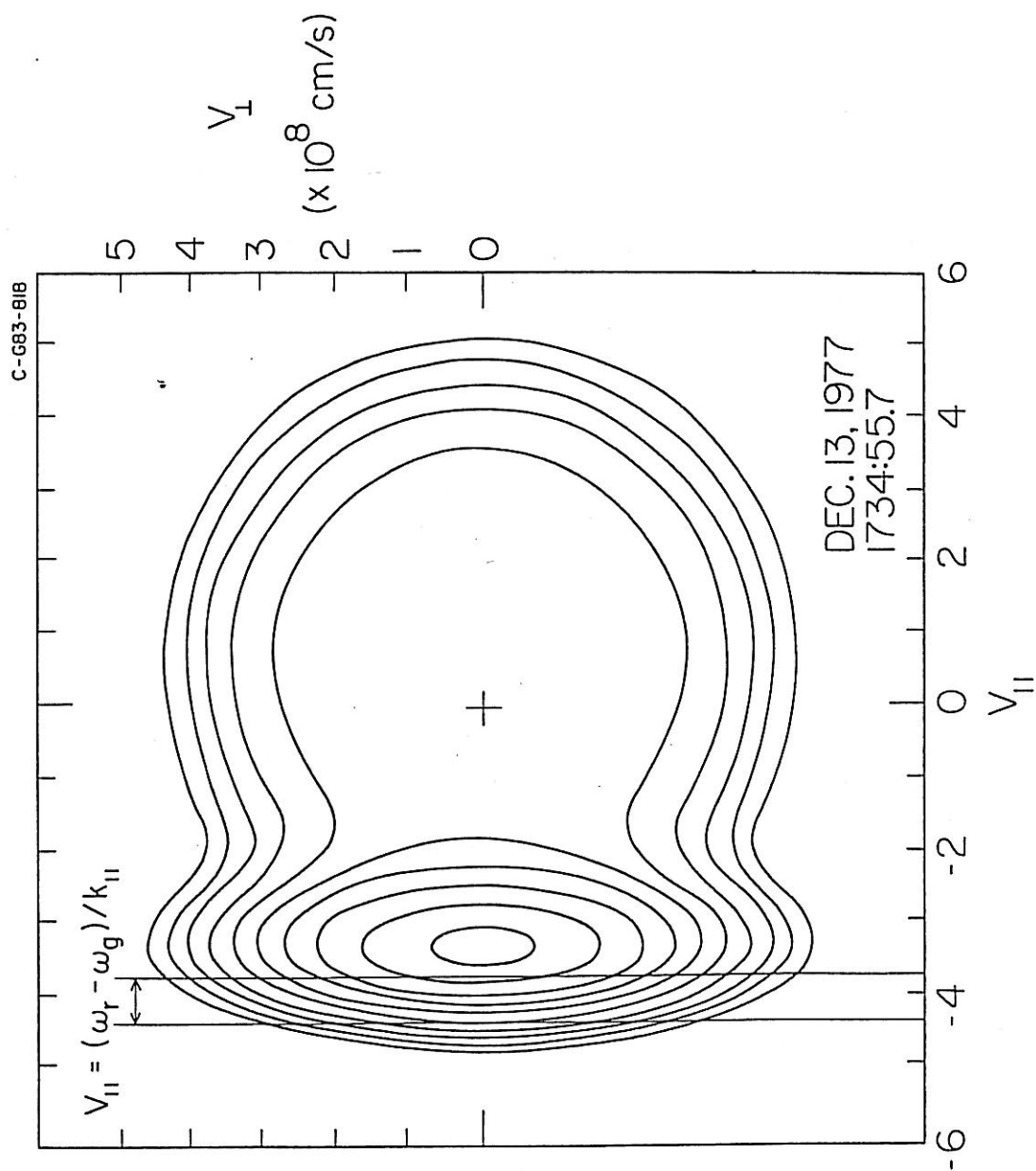


Figure 10

Figure 11

The left column of this figure presents a sample of the growth rates obtained for the electron distribution function measured on October 15, 1978, and for the frequency  $\omega_r/2\pi = 80$  Hz. The unstable waves have  $k_{\parallel} < 0$ , corresponding to wave vectors directed toward the magnetosheath. The top left panel shows the  $m = 0$  Landau contribution to the growth rate while the bottom left panel shows the  $m = +1$  cyclotron contribution to the growth rate. For this frequency and these wave normal angles the  $m = -1$  cyclotron contribution to  $\omega_i/\omega_r$  is negative and negligible. The right column depicts both the  $m = 0$  Landau resonance velocity and the  $m = +1$  cyclotron resonance velocity as a function of the wave normal angle.

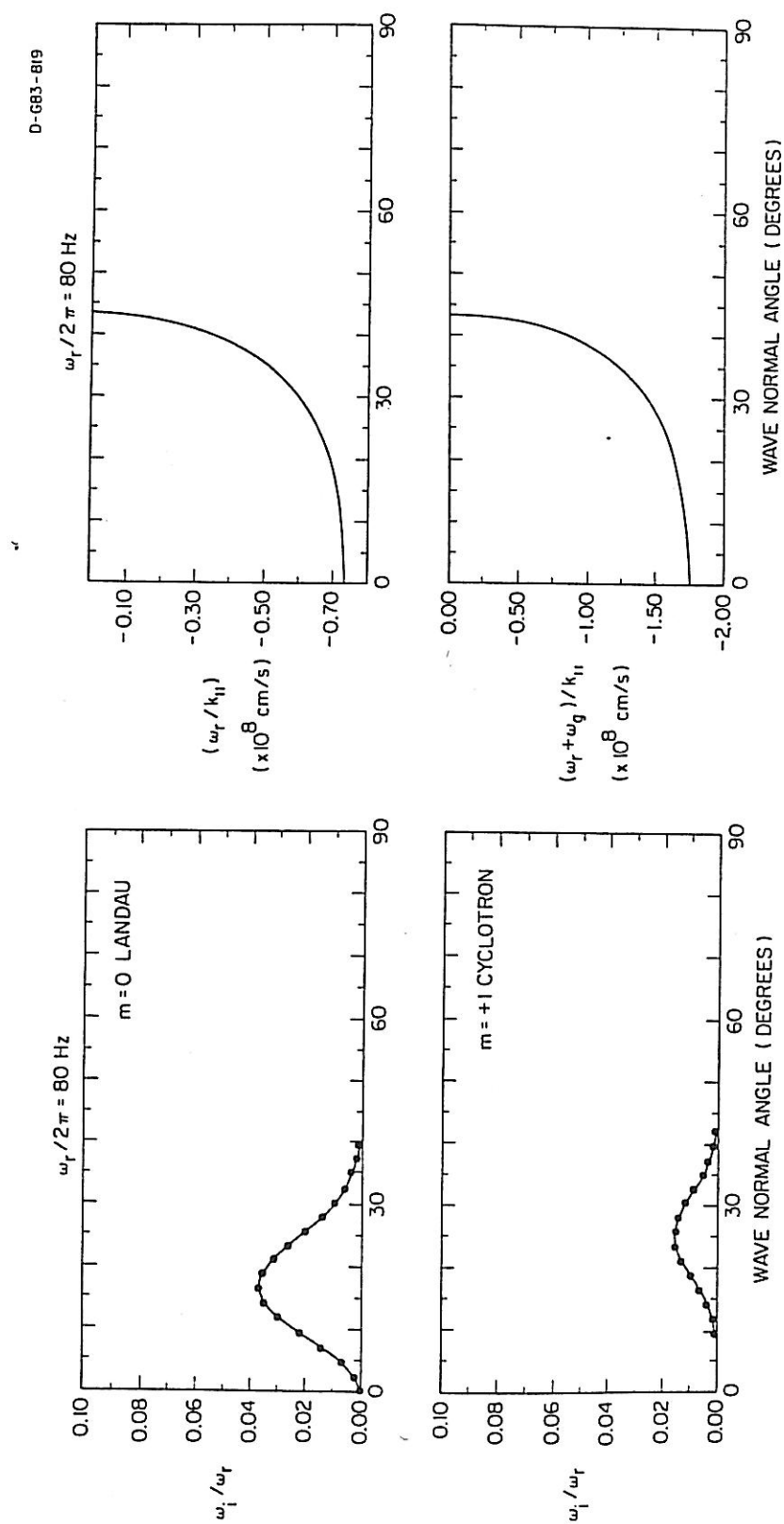


Figure 11

Figure 12

In this figure, the range in the  $m = 0$  Landau and the  $m = +1$  cyclotron resonance velocities corresponding to instability for the case  $\omega_r/2\pi = 80$  Hz, as obtained from Figure 4, is overlayed on a contour plot of the electron distribution function measured on October 15, 1978. The  $m = 0$  Landau resonance velocities lie in regions of positive  $\frac{k_{\parallel}}{|k_{\parallel}|} \frac{\partial F}{\partial v_{\parallel}}$  while the  $m = +1$  cyclotron resonance velocities lie in a region of large anisotropy,  $\frac{\partial F}{\partial \alpha} > 0$ .

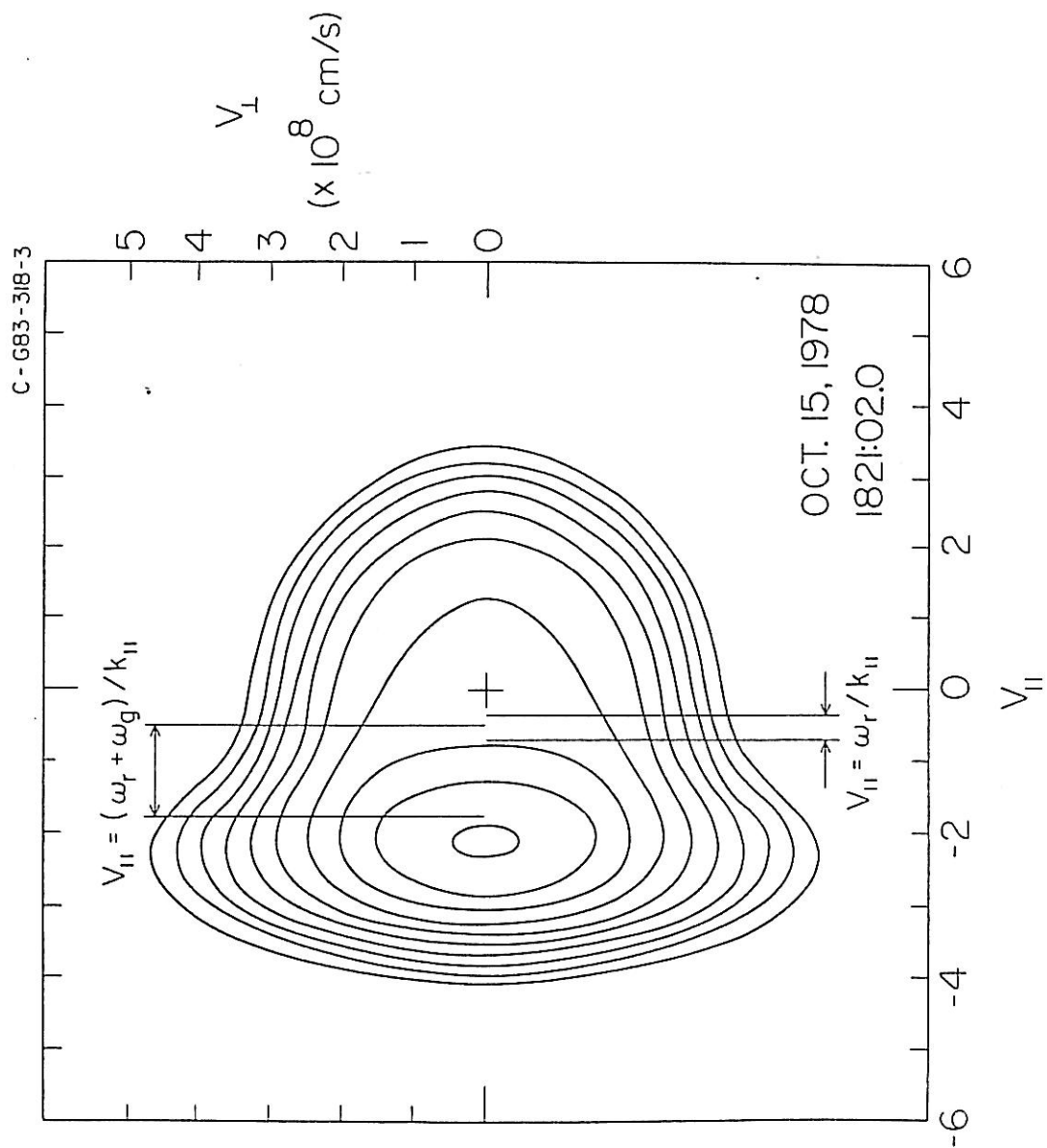


Figure 12

Figure 13

This figure depicts the unstable frequencies and wave normal angles for the October 15, 1978, measured distribution and the case of generation via the  $m = 0$  and  $+1$  resonances. A broad spectrum of frequencies, ranging from about 1 to 100 Hz, is unstable. The unstable wave normal angles range from  $0^\circ$  to the resonance cone angle. For a given frequency, the range of unstable wave normal angles is consistent with locating the resonance velocities in the free energy regions of the distribution.



C-G83-821-2

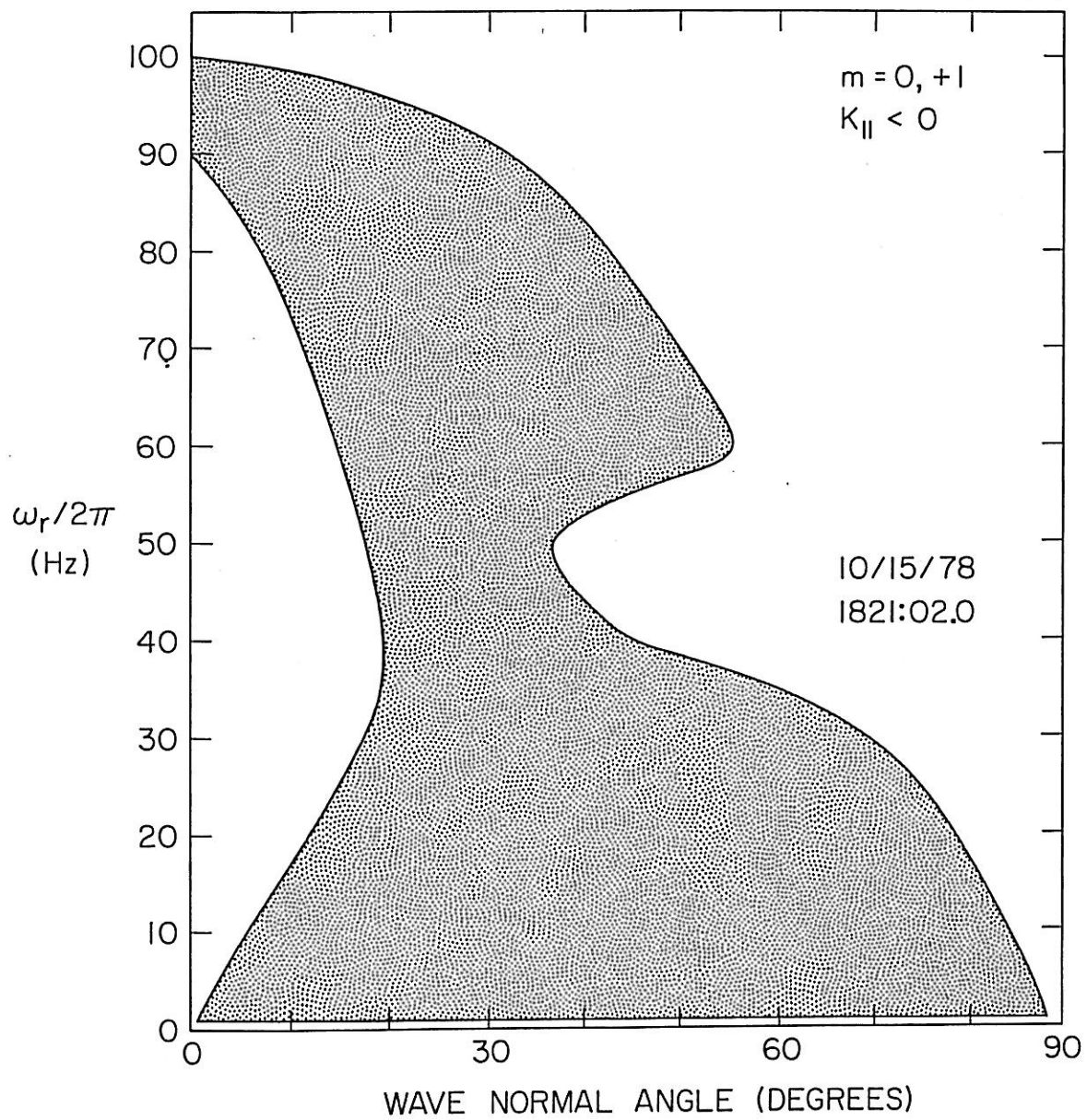


Figure 13

Figure 14

This figure depicts the unstable frequencies and wave normal angles for the three measured distributions and the case of generation via the  $m = -1$  resonance. In many cases, for a given frequency a wide range of wave normal angles is unstable. The unstable frequencies and wave normal angles locate the normal cyclotron resonance velocity in regions of anisotropy associated with the electron beam.

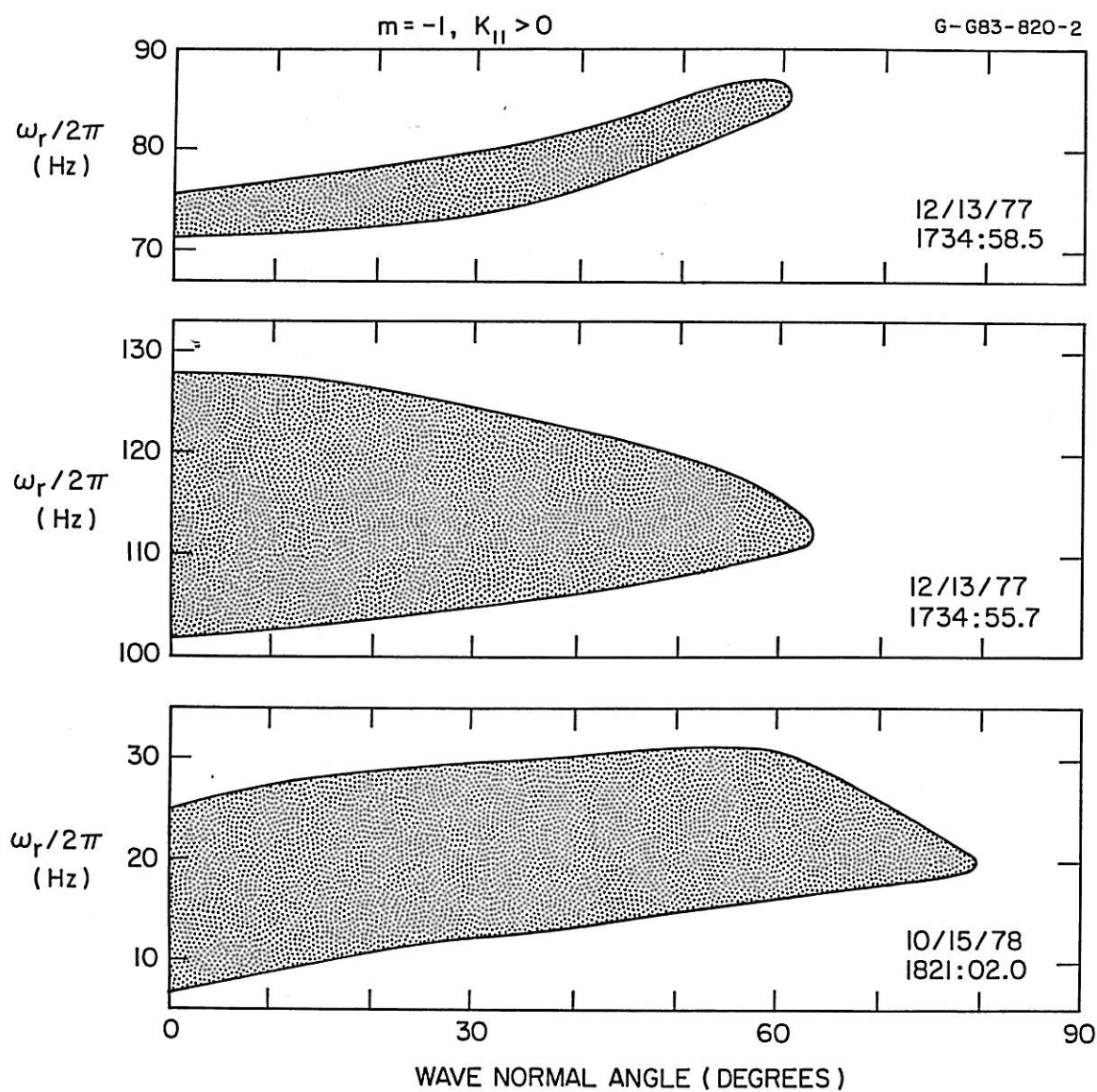


Figure 14

Figure 15

This figure summarizes the unstable frequencies as a function of shock penetration for the model distribution and generation via the  $m = 0$  and  $+1$  resonances. It is usually the case that for a given frequency a wide range of wave normal angles is unstable. The distribution is stable for  $z$  greater than about 50 km because  $\frac{k_{\parallel}}{|k_{\parallel}|} \frac{\partial F}{\partial v_{\parallel}}$  evaluated at the Landau resonance velocity is not sufficiently positive.

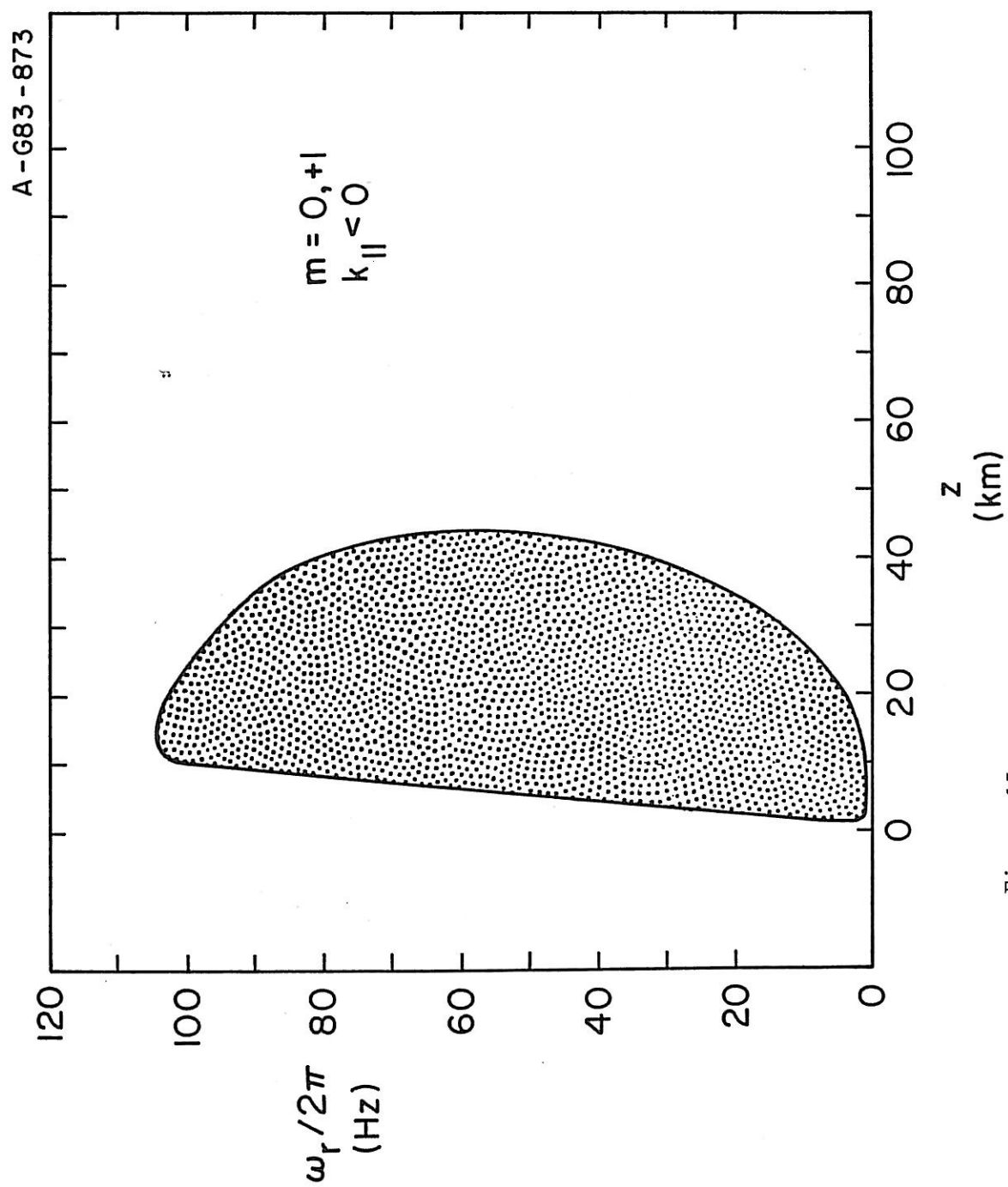


Figure 15

Figure 16

This figure summarizes the unstable frequencies as a function of shock penetration for the model distribution and generation via the  $m = -1$  resonance. The increase in frequency with increasing  $z$  is due to the fact that the normal cyclotron resonance velocity must remain in regions of large anisotropy in  $F(z)$ . As in the case of the measured distributions, for many of the unstable frequencies a wide range of wave normal angles is unstable.

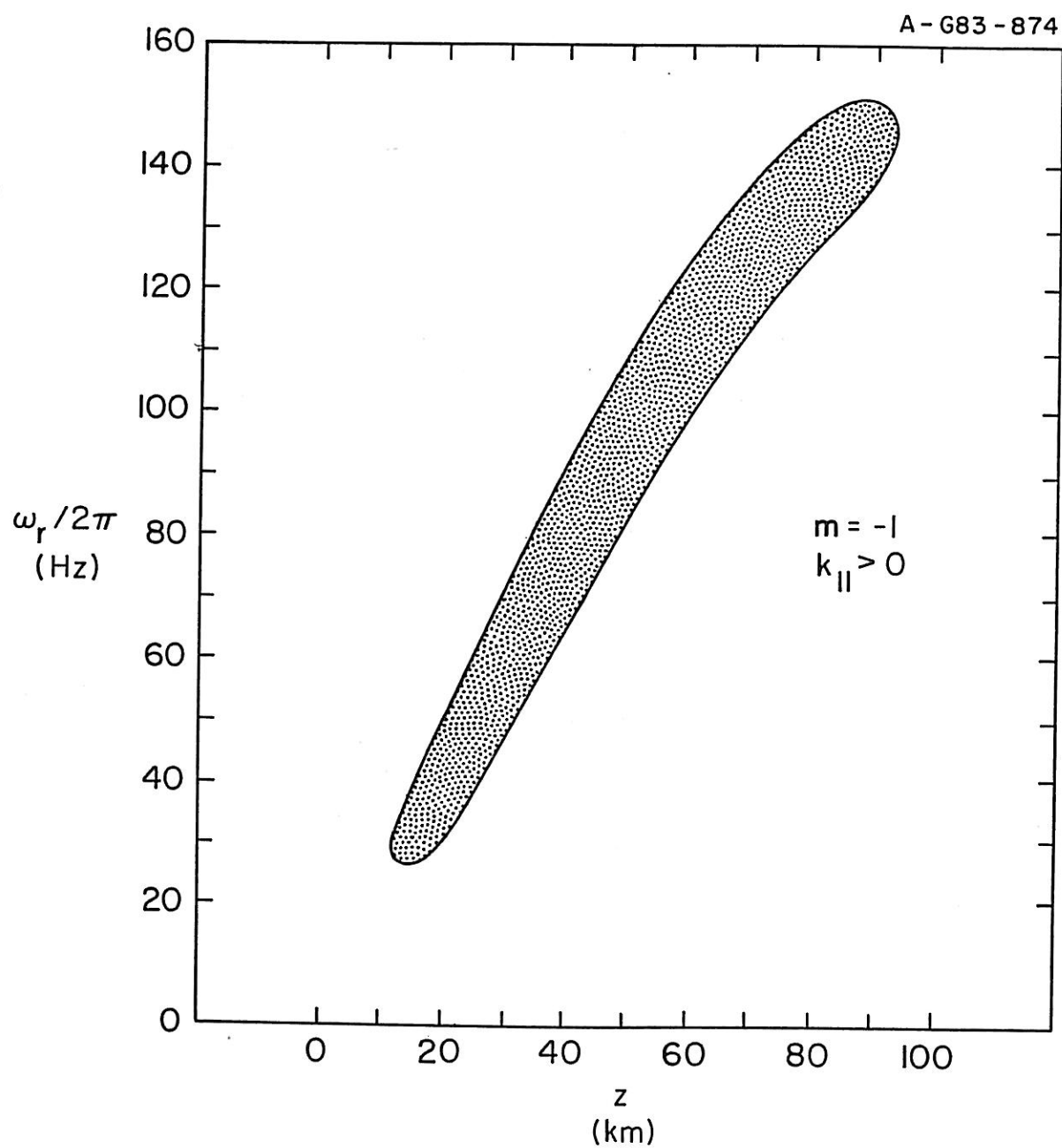


Figure 16

Figure 17

This figure depicts the planar bow shock model used in the ray tracing calculations. The shock transition region extends for 100 km in the  $\hat{z}$  direction and separates the upstream solar wind from the downstream magnetosheath. Within the shock transition, the plasma flow velocity is taken to be the solar wind velocity,  $\vec{v}_{sw} = 400 \hat{z}(\text{km/s})$ . The upstream angle between the magnetic field and the shock normal is taken to be  $45^\circ$ . Due to the planar geometry, the component of  $\vec{B}$  in the direction of  $\hat{n}$  is constant throughout the transition region. The magnetic field magnitude increases linearly with increasing  $z$ . A magnetic field line is shown as are  $B(z)$  and  $\theta_{Bn}(z)$  at  $z = 70 \text{ km}$ .



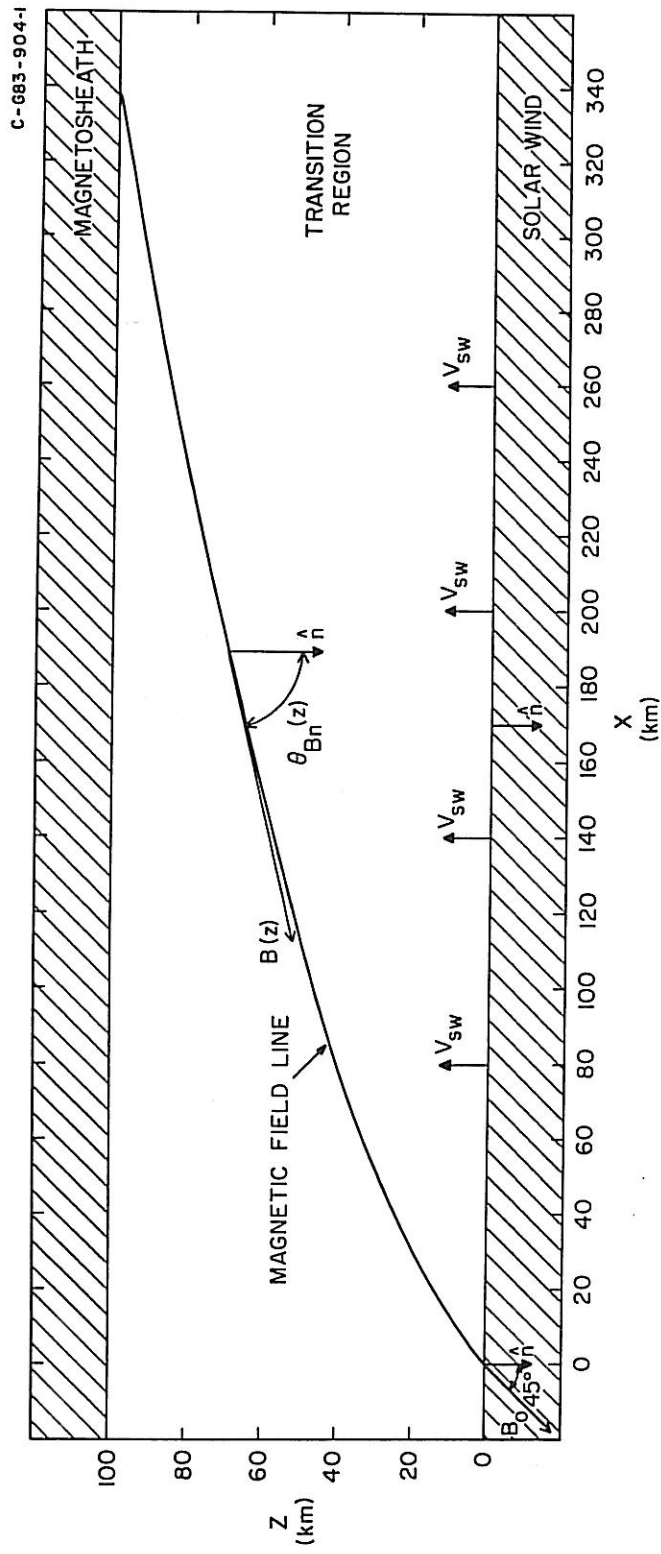


Figure 17

Figure 18

This figure illustrates the relative orientations of the magnetic field vector, the wave vector, the group velocity, and the solar wind velocity for the case of  $k_{\parallel} < 0$ . All vectors lie in the plane of the figure. Of the cone of unstable wave vectors, two are distinguished by the angle  $\phi$  with the  $\phi = 0^\circ$  direction defined to be towards the solar wind. The  $\phi = 180^\circ$  orientation lies on the unstable cone and is  $180^\circ$  in azimuth from the  $\phi = 0^\circ$  orientation. For a given wave vector orientation, the ray path direction in the shock frame of reference is in the direction of the vector  $\vec{v}_g + \vec{v}_{sw}$ . For  $k_{\parallel} < 0$ , the ray paths are directed toward the magnetosheath.

A-683-905

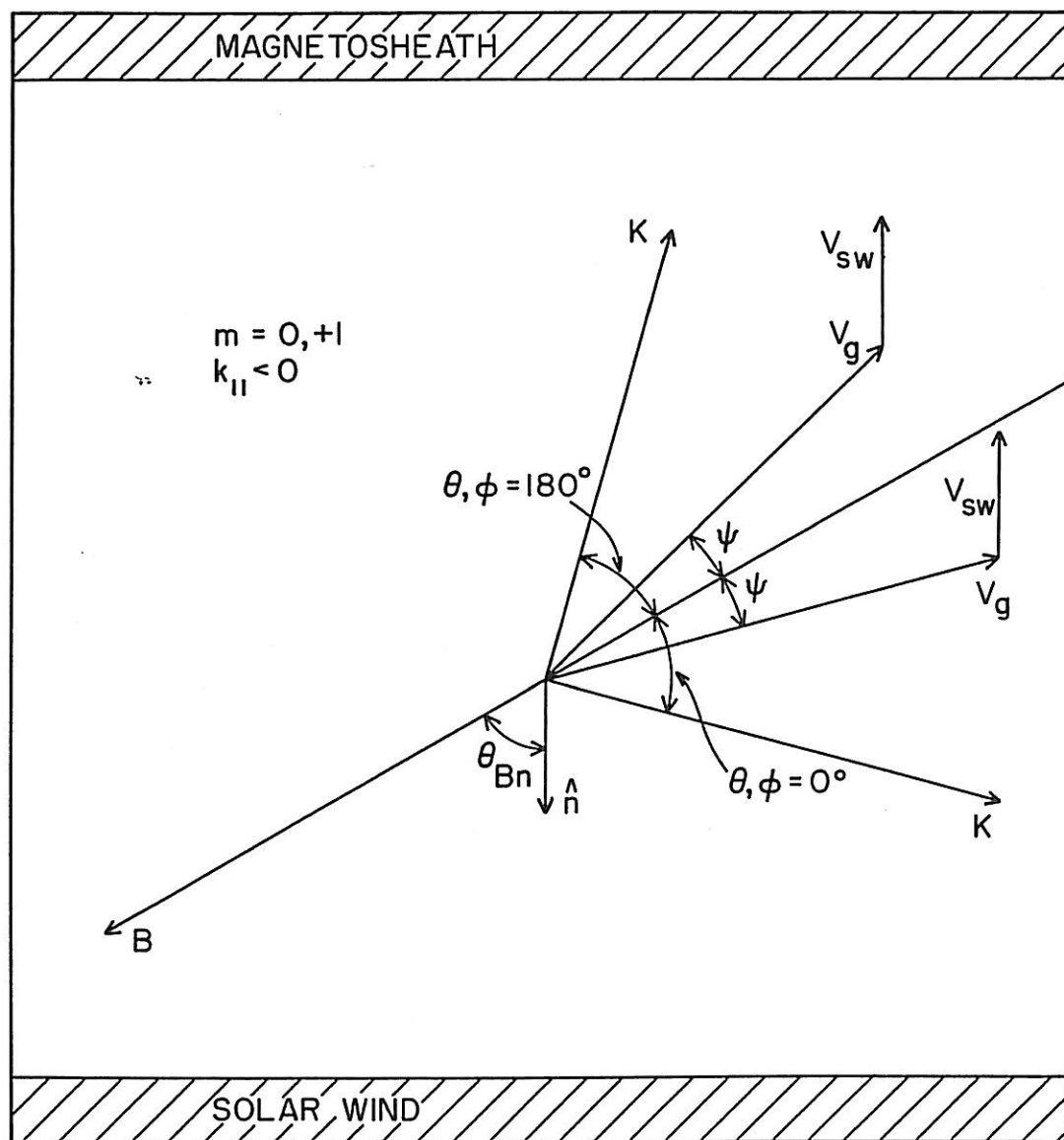


Figure 18

Figure 19

This figure is similar to Figure 19 but illustrates the geometry for the case  $k_{\parallel} > 0$ . The ray path directions in the shock frame are given by the direction of the vector  $\vec{v}_g + \vec{v}_{sw}$ . In the majority of cases, the ray path is directed toward the solar wind. However, the figure illustrates that for oblique wave normal angles and the  $\phi = 180^\circ$  orientation the ray path can be in the direction of the solar wind.

A-G83-906-1

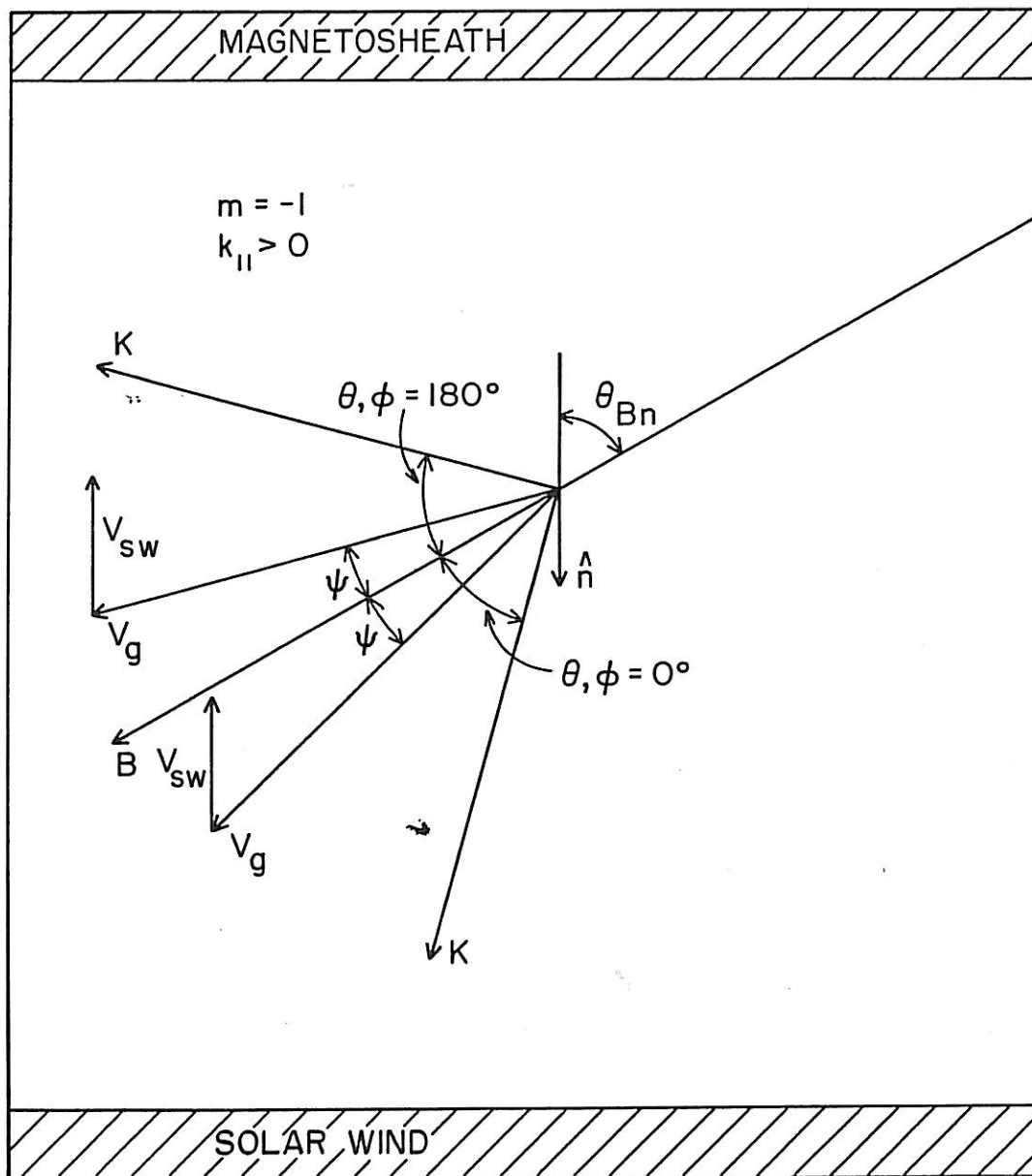


Figure 19

Figure 20

This figure summarizes the results of the ray tracing calculations. Shown are a magnetic field line and several ray paths in the shock transition region. The ray paths for generation via the  $m = 0$  and  $+1$  resonances originate in the lower left corner of the figure while those for generation via the  $m = -1$  resonance originate on the right side of the figure. The ray paths are labeled in the format  $(\omega_r/2\pi, \theta_0, \phi)$  where  $\theta_0$  and  $\phi$  specify the initial wave vector orientation. A  $\phi$  value for  $\theta_0 = 0^\circ$  is not applicable and so is omitted from the ray path labels. At the heads of the arrows denoting the ray path, the integrated growth along the ray path,  $\Gamma$ , is given. The ray paths terminate when the growth rate becomes negative.

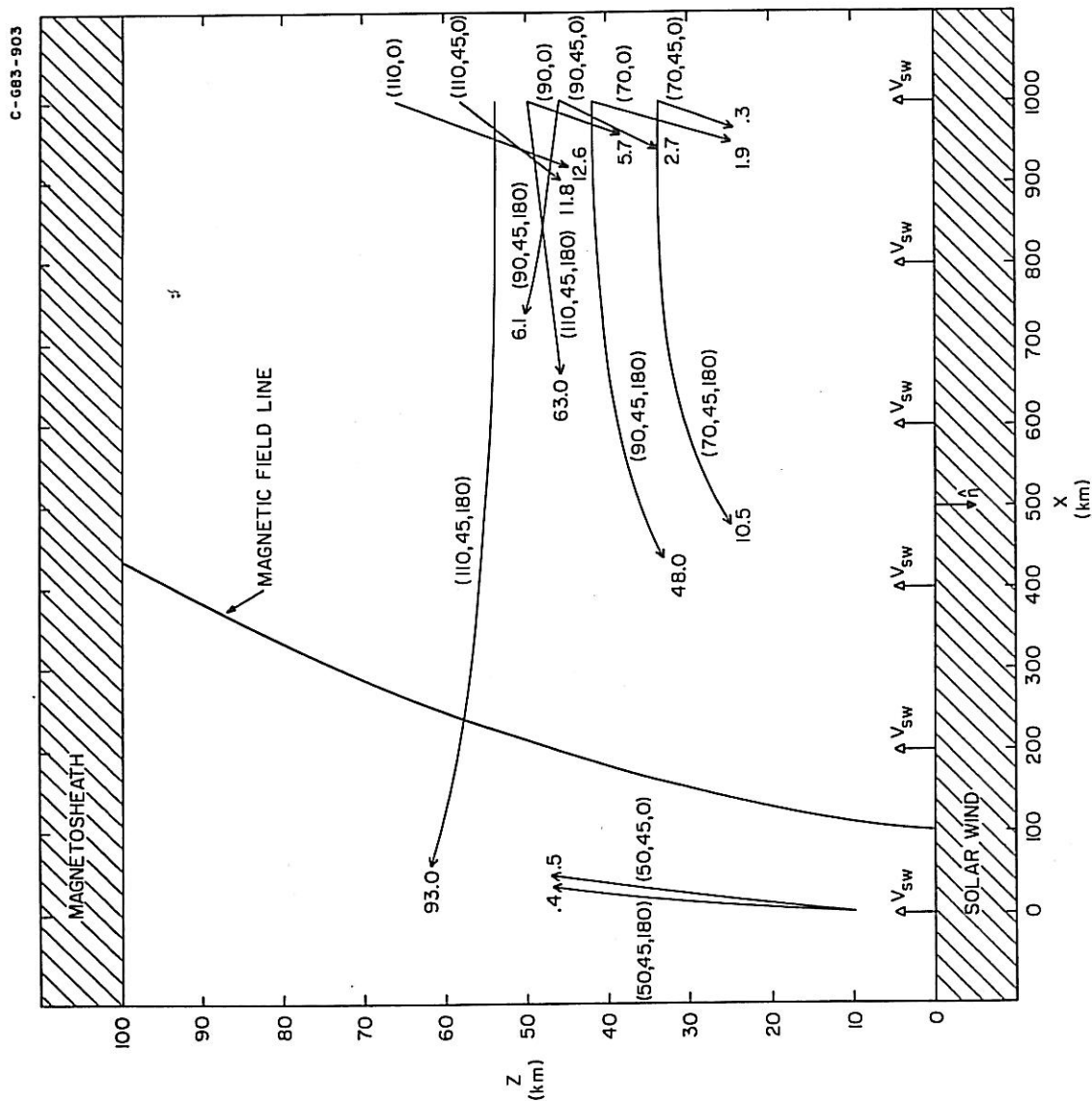


Figure 20

## REFERENCES

- Bame, S. J., J. R. Asbridge, H. E. Felthouser, J. P. Glore, G. Paschmann, P. Hemmerich, K. Lehmann, and H. Rosenbauer, ISEE-1 and ISEE-2 fast plasma experiment and the ISEE-1 solar wind experiment, IEEE Trans. Geosci. Electron., GE-16, 216, 1978.
- Bame, S. J., J. R. Asbridge, J. T. Gosling, M. Halbig, G. Paschmann, N. Sckopke, and H. Rosenbauer, High temporal resolution observations of electron heating at the bow shock, Space Sci. Rev., 23, 75, 1979.
- Budden, K. G., Radio Waves In the Ionosphere, Cambridge Press, 1961.
- Feldman, W. C., R. C. Anderson, S. J. Bame, S. P. Gary, J. T. Gosling, D. J. McComas, M. F. Thomsen, G. Paschmann, and M. M. Hoppe, Electron velocity distributions near the Earth's bow shock, J. Geophys. Res., 88, 96, 1983.
- Feldman, W. C., S. J. Bame, S. P. Gary, J. T. Gosling, D. McComas, M. F. Thomsen, G. Paschmann, N. Sckopke, M. M. Hoppe, and C. T. Russell, Electron heating within the Earth's bow shock, Phys. Rev. Lett., 49, 199, 1982.
- Formisano, V., The potential drop across Earth's bow shock, Geophys. Res. Lett., 9, 1033, 1982.
- Forslund, D. W., J. M. Kindel, and M. A. Strosio, Current driven electromagnetic ion cyclotron instability, J. Plasma Phys., 21, 127, 1979.
- Fredricks, R. W., C. F. Kennel, F. L. Scarf, G. M. Crook, and I. M. Green, Detection of electric-field turbulence in the earth's bow shock, Phys. Rev. Lett., 21, 1761, 1968.
- Greenstadt, E. W., and R. W. Fredricks, Shock systems in collisionless space plasmas, in Solar System Plasma Physics, Vol III, ed. by C. F. Kennel, L. J. Lanzerotti, and E. N. Parker, North-Holland Publishing Company, 1979.
- Gurnett, D. A., F. L. Scarf, R. W. Fredricks, and E. J. Smith, The ISEE 1 and ISEE 2 plasma wave investigation, IEEE Trans. Geosci. Electron., GE-16, 225, 1978.



- Holzer, R. E., M. G. McLeod, and E. J. Smith, Preliminary results from the OGO 1 search coil magnetometer: Boundary positions and magnetic noise spectra, J. Geophys. Res., 71, 1481, 1966.
- Kennel, C. F., Low-frequency whistler mode, Phys. of Fluids, 9, 2190, 1966.
- Kennel, C. F., and H. V. Wong, Resonant particle instabilities in a uniform magnetic field, J. Plasma Physics, 1, 75, 1967.
- Leimohn, H. B., and F. L. Scarf, Whistler attenuation by electrons with an  $E^{-2.5}$  distribution, J. Geophys. Res., 67, 4163, 1962.
- Neubauer, F. M., H. J. Beinroth, H. Barnstorff, and G. Dehmel, Initial results from the Helios-1 search coil magnetometer experiment, J. Geophys. Res., 42, 599, 1977.
- Rodriguez, P., and D. A. Gurnett, Electrostatic and electromagnetic turbulence associated with the Earth's bow shock, J. Geophys. Res., 80, 19, 1975.
- Russell, C. T., The ISEE-1 and -2 fluxgate magnetometers, IEEE Trans. Geosci. Electron., GE-16, 239, 1978.
- Russell, C. T., and E. W. Greenstadt, Initial ISEE magnetometer results: Shock observations, Space Sci. Rev., 23, 3, 1979.
- Sentman, D. D., M. F. Thomsen, S. P. Gary, W. C. Feldman, and M. M. Hoppe, The oblique whistler instability in the Earth's foreshock, J. Geophys. Res., 88, 2048, 1983.
- Stix, T. H., The Theory of Plasma Waves, McGraw-Hill, 1962.
- Tokar, R. L., and D. A. Gurnett, Propagation characteristics of whistler mode waves generated by electron beams in Earth's bow shock, to be submitted to J. Geophys. Res., 1984.
- Tokar, R. L., D. A. Gurnett, and W. C. Feldman, Whistler mode turbulence generated by electron beams in Earth's bow shock, accepted for publication in J. Geophys. Res., 1983.